Graduate School ETD Form 9
(Revised 12/07)

PURDUE UNIVERSITY
GRADUATE SCHOOL
Thesis/Dissertation Acceptance

This is to certify that the thesis/dissertation prepared

By Chan Xiao

Entitled COMPUTATIONAL STUDY OF SURFACE-SEGREGATED PT ALLOY CATALYSTS FOR OXYGEN REDUCTION REACTION

For the degree of Master of Science in Mechanical Engineering

Is approved by the final examining committee:

Guofeng Wang
Chair

Hazim El-Mounayri

Rongrong Chen

To the best of my knowledge and as understood by the student in the *Research Integrity and Copyright Disclaimer (Graduate School Form 20)*, this thesis/dissertation adheres to the provisions of Purdue University's "Policy on Integrity in Research" and the use of copyrighted material.

Approved by Major Professor(s): Guofeng Wang

Approved by: Jie Chen 06/29/2010
Head of the Graduate Program Date

Graduate School Form 20
(Revised 1/10)

PURDUE UNIVERSITY
GRADUATE SCHOOL

Research Integrity and Copyright Disclaimer

Title of Thesis/Dissertation:
COMPUTATIONAL STUDY OF SURFACE-SEGREGATED PT ALLOY CATALYSTS FOR OXYGEN REDUCTION REACTION

For the degree of Master of Science in Mechanical Engineering

I certify that in the preparation of this thesis, I have observed the provisions of *Purdue University Teaching, Research, and Outreach Policy on Research Misconduct (VIII.3.1)*, October 1, 2008.*

Further, I certify that this work is free of plagiarism and all materials appearing in this thesis/dissertation have been properly quoted and attributed.

I certify that all copyrighted material incorporated into this thesis/dissertation is in compliance with the United States' copyright law and that I have received written permission from the copyright owners for my use of their work, which is beyond the scope of the law. I agree to indemnify and save harmless Purdue University from any and all claims that may be asserted or that may arise from any copyright violation.

Chan Xiao
Printed Name and Signature of Candidate

06/29/2010
Date (month/day/year)

*Located at http://www.purdue.edu/policies/pages/teach_res_outreach/viii_3_1.html

COMPUTATIONAL STUDY OF SURFACE-SEGREGATED PT ALLOY CATALYSTS FOR OXYGEN REDUCTION REACTION

A Thesis
Submitted to the Faculty
of
Purdue University
by
Chan Xiao

In Partial Fulfillment of the
Requirements for the Degree
of
Master of Science in Mechanical Engineering

August 2010
Purdue University
Indianapolis, Indiana

ACKNOWLEDGEMENTS

This thesis is dedicated to my parents.

First, I would like to show my great gratitude to my research advisor Dr. Guofeng Wang for his valuable guidance and supervision in every stage of my research. Without the generous sharing of his research experience and knowledge, enlightening instruction and patience, this thesis would not be possible. Dr. Wang's keen and rigorous attitude toward science and research will always inspire me.

I would also like to thank Dr. Hazim EI-Mounayri and Dr. Rongrong Chen for being my advisory committee members. Their insights and comments helped me make this thesis better.

I would like to extend my special thanks to my group members: Zhouwen Chen, Joseph Heidenreich, Zhiyao Duan, Jun Zhong, Yuhua Zhang, Qing Peng and Sachin Terdalkar for their useful suggestion and critiques on my thesis defense powerpoint preparation. Moreover, I have learned a lot of knowledge and software techniques from them which are very helpful during the whole research process.

Last but not least, I would like to thank all my friends here for their encouragement and company in time of need.

TABLE OF CONTENTS

Page

LIST OF TABLES

Table Page

LIST OF FIGURES

Figure Page

ABSTRACT

Xiao, Chan. M.S.M.E., Purdue University, August 2010. Computational Study of Surface-segregated Pt Alloy Catalysts for Oxygen Reduction Reaction. Major Professor: Guofeng Wang.

In this thesis two research objectives have been accomplished using computational simulation techniques. (1) The surface segregation phenomena in the surfaces of (111), unreconstructed (110) and reconstructed (1x2) missing row (110) surfaces of Pt-Ni and Pt-Co disordered alloys have been accurately predicted using Monte Carlo (MC) simulation method, and (2) the configuration and energy of the adsorption of O, O_2, OH, and H_2O molecules which are presented in oxygen reduction reaction (ORR) on the surface of pure Pt and surface-segregated Pt-binary alloys (i.e., Pt-Ni, Pt-Co and Pt-Fe) have been determined using density functional theory (DFT) calculations. This thesis yields some guiding principles for designing novel catalysts for proton exchange membrane fuel cells.

The Pt concentration profiles of the surfaces of Pt-Ni and Pt-Co alloys were attained from the MC simulations in which the system energy was evaluated through the developed modified embedded atom method (MEAM) for Pt-Ni and Pt-Co alloys. It was found from our simulations that the Pt atoms strongly segregate to the outermost layer and the Ni atoms segregate to the second sub-layer in the (111) surface of both Pt-Ni and Pt-Co alloys. When Pt concentration is higher than 75 at.%, pure Pt top layer could be formed in the outermost layer (111) surface of both alloys. Moreover, segregation reversal phenomenon (Ni atoms segregating to the outermost layer while Pt atoms to the second sub-layer) was observed in our MC simulations of unreconstructed (110) surface

of Pt-Ni alloys. In contrast, a Pt enriched outermost surface layer was found in a Pt-Ni reconstructed (1x2) missing row (110) surface. Our MC simulation results agree well with published experimental observations.

In addition, adsorption of atomic and molecular oxygen, water and hydroxyl on the (111) and (100) surfaces of pure Pt and Pt-based alloys (Pt-Ni, Pt-Co and Pt-Fe) were studied using spin DFT method and assuming a coverage of 0.25 monolayer. Both the optimized configurations and the corresponding adsorption energies for each species were obtained in this study. In particular, we elucidated the influence of the adsorption energies of atomic oxygen and OH on the activity for ORR on Pt binary alloy catalysts in acidic environment. The calculated adsorption energies of atomic oxygen on the (111) surfaces of pure Pt, Pt-Ni, Pt-Co and Pt-Fe are -3.967 eV, -3.502 eV, -3.378 eV and -3.191 eV, respectively. The calculated adsorption energies of hydroxyl on the (111) surfaces of pure Pt, Pt-Ni, Pt-Co and Pt-Fe are -2.384 eV, -2.153 eV, -2.217 eV and -2.098 eV, respectively. The interaction between the adsorbed atomic and hydroxyl and the corresponding (111) surface becomes weaker for the surface-segregated alloys compared to pure Pt catalyst. The same results were obtained for the (100) surfaces.

1. INTRODUCTION

1.1 Background

1.1.1 PEMFC

Fuel cell is electrochemical equipment that can convert chemical energy into electricity. According to the type of electrolyte they use, fuel cells can be classified into alkaline fuel cells (AFC), proton exchange membrane fuel cells (PEMFC), phosphoric acid fuel cells (PAFC), molten carbonate fuel cells (MCFC) and solid oxide fuel cells (SOFC). Table 1.1 lists main properties of each type of fuel cells [1].

Table 1.1 Description of major fuel cell types

Type	PEMFC	PAFC	AFC	MCFC	SOFC
Electrolyte	Polymer membrane	Liquid H_3PO_4	Liquid KOH	Molten carbonate	Ceramic
Charge carrier	H^+	H^+	OH^-	CO_3^{2-}	O^{2-}
Operating temperature	80 ^oC	200 ^oC	60~220 ^oC	650 ^oC	600~1000 ^oC
Catalyst	Platinum	Platinum	Platinum	Nickle	Perovskites (ceramic)
Cell components	Carbon based	Carbon based	Carbon based	Stainless based	Ceramic based
Fuel compatibility	H_2, methanol	H_2	H_2	H_2, CH_4	H_2, CH_4, CO

1.1.1.1 Component of PEMFC

Proton exchange membrane fuel cells, also known as polymer electrolyte membrane fuel cells, are one of the most promising fuel cells that have been commercialized. Figure 1.1 gives out the typical cell stock of PEMFC [2]. The components include: (1) the proton exchange membrane; (2) gas diffusion layer (an electrically conductive porous backing layer); (3) catalyst layer (the electrodes) sandwiched between the membrane and gas diffusion layer; (4) Teflon/rubber/PTFE gaskets for gas sealing and electrical insulation; (5) bipolar plates with gas channels on one side that delivers the fuel and oxidant to the reactive sites; (6) other materials for e.g. interconnecting, cooling, manifold and others. The key part of PEMFC is the membrane electrode assembly (MEA), which consists of a proton exchange membrane with anode and cathode catalyst layers attached onto each surface, two gas diffusion layers contacted with the catalyzed membrane.

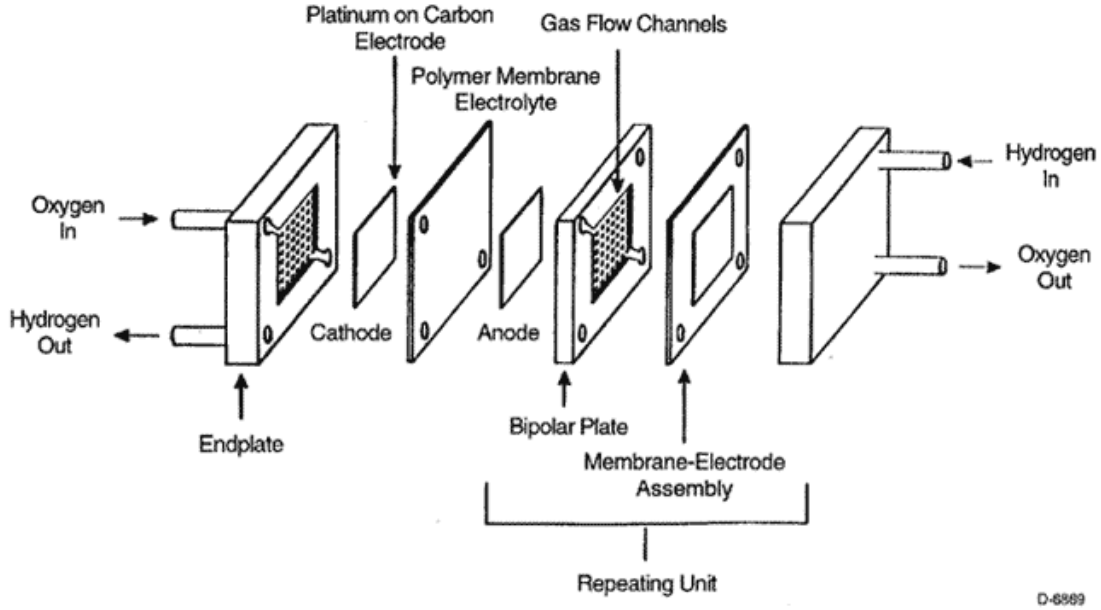

Figure 1.1 Typical PEMFC stack construction

1.1.1.2 Principle of PEMFC

The work of PEMFC starts with hydrogen splitting into the anode (negative electrode). Then hydrogen will release proton and electron on catalyst (e.g. platinum particles). The resulting protons then diffuse through the proton-conducting polymer membrane to the cathode (positive electrode), while the electrons pass as current through the external circuit to the cathode. The protons then recombine at the cathode with the electrons and with oxygen on catalyst (e.g. platinum particles) to produce electricity, heat and water. The basic reactions taken place in the PEMFC are described in Eq. 1.1 - 1.3.

At the anode:

$$H_2 \rightarrow 2H^+ + 2e^- \qquad \text{Eq. 1.1}$$

At the cathode:

$$1/2O_2 + 2H^+ + 2e^- \rightarrow H_2O \qquad \text{Eq. 1.2}$$

Overall:

$$1/2O_2 + H_2 \rightarrow H_2O \qquad \text{Eq. 1.3}$$

As for a single PEMFC, the voltage is 0.5 to 1.0 V. By combining a number of single cells into a stack, an appropriate voltage level for a specific application would be achieved.

1.1.1.3 ORR and Pt-based Alloys

Oxygen reduction reaction (ORR) is the most important reaction in PEMFC. Happened at the cathode, there are five possible pathways of ORR as shown in Figure 1.2 [3]:

1) a “direct” 4-electron pathway with oxygen molecule combining with four ions and four electrons to form water;
2) a 2-electron reduction pathway with oxygen reduced to hydrogen peroxide;
3) a “series” pathway with 2-electron reduction to peroxide and 4-electron to water;

4) a “parallel” pathway which is combined with 1), 2) and 3);

5) an “interactive” pathway where species diffused from a “series” pathway into a “direct” pathway.

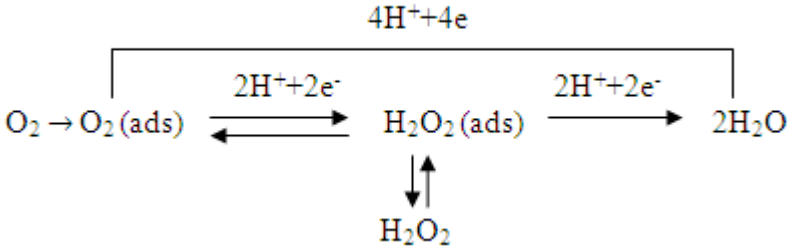

Figure 1.2 ORR pathways

The performance of PEMFC is limited by the kinetic sluggish of ORR, so researchers and developers are trying to find promising catalysts to speed up the ORR kinetics and making PEMFC to a more usable level. At present, the most practical catalysts for ORR are Pt-based catalysts. Alloying other metal elements (usually transition metals) with Pt not only reduce the Pt loading in catalyst layers, but also improve the catalytic activity.

There are two mechanisms for ORR on Pt suggested by theoretical studies based on DFT. One is the dissociative mechanism for reactions taken place in the low current density range; the other is the associative mechanism which is proposed for a high current density range [4 - 5].

Dissociative mechanism can be expressed as Eq. 1.4 - 1.6:

$1/2O_2 + * \rightarrow O*$ Eq. 1.4

$O* + H^+ + e^- \rightarrow OH*$ Eq. 1.5

$$OH^* + H^+ + e^- \rightarrow H_2O + * \quad \text{Eq. 1.6}$$

were * represents the adsorption site on the surface of Pt. Since there is no H_2O_2 produced, this mechanism can be treated as the direct 4-electron pathway. Oxygen molecule is divided into two oxygen atoms in the process of adsorption. The adsorbed oxygen atoms combine with ions and electrons to form water.

Associative mechanism can be described as Eq. 1.7 - 1.11.

$$1/2O_2 + * \rightarrow O_2^* \quad \text{Eq. 1.7}$$

$$O_2 {}^*+ H^+ + e^- \rightarrow HO_2^* \quad \text{Eq. 1.8}$$

$$HO_2^* + H^+ + e^- \rightarrow H_2O + O^* \quad \text{Eq. 1.9}$$

$$O^* + H^+ + e^- \rightarrow OH^* \quad \text{Eq. 1.10}$$

$$OH^*+H^+ + e^- \rightarrow H_2O + * \quad \text{Eq. 1.11}$$

Instead of breaking the O-O bond, the associative mechanism starts with the oxygen molecule adsorbed on the Pt surface. This process can be regarded as another expression of Figure 1.2. H_2O_2 doesn't appear in the mechanism, but it can be formed with the adsorbed O_2 then further reduced to H_2O or be a final product.

Though Pt-based alloys are considered as the best catalysts for ORR in PEMFC at the current technology level, extensive efforts have been made to develop alternative catalysts because of the limited storage in the earth and high price of Pt which make PEMFC less competitive in the marketplace. For example, non-noble metal catalysts, carbon materials, quinine and derivatives, transition metal macrocyclic compounds, transition metal chalcogenides, and transition metal carbides [6].

1.1.2 Surface Segregation

1.1.2.1 Definition

Surface is not only the boundary that separates the solid from its environment, but a region that most physical and chemical phenomena occur. Many alloys exhibit different surface properties from the bulk. One of them is called surface segregation. By definition, surface segregation is a phenomenon that one or more types of elements enrich in the surface region, resulting in the surface composition becoming higher than the bulk composition. This phenomenon is of great importance, especially for catalyst study, because it may either improve or obstruct desirable and undesirable reactions. There are two types of segregation in binary alloy [7]. One is so-called solute segregation when the minority component of the two metals enrich at the surface. The other is solvent segregation when the majority component is more concentrated at the surface. Surface segregation attracts a lot of interest, especially in the field of fuel cell catalyst; because most of the catalysts are alloys and the surface concentration of each element as well as the structure greatly influence the catalytic activities.

1.1.2.2 Experimental and Theoretical Methods

The thermodynamics of surface segregation was first studied by Willard Gibbs [7] about one century ago. After one hundred years of development, this field Nowadays there are several experimental methods to obtain the surface concentrations: ion scattering spectroscopy (ISS), auger electron spectroscopy (AES), X-ray photoemission spectroscopy (XPS), atom-probe field-ion microscopy (APFIM) and low-energy electron diffraction (LEED). XPS and AES are two conventional tools to study segregation, which obtain an average composition with respect to the probing depth. Limited by the depth resolution, these two methods cannot give composition at a specific layer, and the procedure is quite complex as well. APFIM and ISS have been applied to investigate the segregation phenomenon on the surface for ordered alloys. By using LEED we can obtain the concentration profile up to the fourth layer.

Although the development of experimental techniques enables us to a wide and deep exploration of surface segregation for catalysts, limitations still exist because of:

1) the expensive cost of those big equipments and labor cost of maintenance;
2) difficulties in preparing experimental samples, especially the ideal case which requires clean surface.

Thus, theoretical modeling for surface segregation as an important aspect has been widely applied.

The theoretical study for surface segregation includes two aspects: first is the energy evaluation by atomic interaction model such as modified embedded atom method (MEAM), or electronic structures based on first principles; second is the statistical approximation to determine the equilibrium properties of the energy evaluation model, which is normally conducted by Monte Carlo (MC) simulation. The advantage of MEAM over traditional lattice-gas model (also called bond-breaking model) is that it takes environment dependence into consideration, meaning the atoms on the surface experience bond energies different from the atoms in the bulk.

1.1.2.3 Mechanism for Surface Segregation

Two factors have great influence in determining which element of the binary alloy system may segregate to the surface or stay away from the surface. The first factor is size effect. Due to the atomic size difference between the two elements in the binary alloy, the mismatch strain energy of the system might be decreased when one element diffuse towards the surface, compared to when the two elements are randomly distributed in the alloy system. The difference between surface energies of pure elements is the other reason causing surface segregation. The element with lower surface energy will diffuse towards the surface and thus decrease the total surface energy of the binary alloy system. Sometimes the effects of atomic size difference and the relative surface energies may cause different element segregation so they are in close competition with each other to determine the final segregation structure. The most interesting case is the surface

orientation-dependent segregation of Pt-Ni disordered alloys, which is in detailed discussion in this thesis.

1.2 Objectives

There were two main objectives in this research: (1) to investigate the surface segregation phenomenon of Pt-Ni and Pt-Co alloys system by using MC simulation method with potentials developed by MEAM; (2) to compare the ORR catalytic activity of pure Pt to Pt-Ni, Pt-Co and Pt-Fe alloys through analysis of adsorption energy of ORR intermediates on the surface of pure Pt and Pt-based alloys. These two objectives were not totally independent with each other. We want to explore the surface structures of Pt-based alloys at first, which may affect the catalytic activity for ORR. After the surface structures were determined, we were able to further study the catalytic performance of those alloys with particular surface properties in ORR process. The overall aim of this research is to provide some guidance for the novel catalyst design in PEMFC.

The most close-packed (111) surface of disordered Pt_xNi_{100-x} and Pt_xCo_{100-x} alloys were studied at the temperature of 1200 K. The segregation files were obtained as a function of bulk Pt concentration and compared with experimental data to verify the reliability of our MC model. Further investigation was done for Pt_xNi_{100-x} unreconstructed (110) surface at the temperature at 1200 K and reconstructed (1x2) missing row (110) surface at 1000 K, 1200 K and 1400 K. Interlayer relaxations of disordered Pt_xNi_{100-x} alloys during segregation were calculated to find out some clues for the orientation dependent surface segregation.

The adsorption system of single oxygen atom, hydroxyl, water molecule and oxygen molecule on the (111) and (100) surfaces of pure Pt and Pt-Ni, Pt-Co and Pt-Fe alloys were studied by DFT. By evaluating the adsorption energies on different adsorption sites, the most stable configuration for each adsorbate can be obtained. Besides providing clear trends regarding adsorption tendency on different sites, we also

focused on the influence of adsorption energies of OH and O_2 on the catalytic activity in acid environment.

1.3 Organization

Five chapters are covered in the thesis to provide a complete and clear picture about the project. The background knowledge about PEMFC and surface segregation is provided in Chapter 1. We introduce the component and principle of PEMFC, and emphasize mechanism of the ORR which is the bottleneck of PEMFC. For the surface segregation, a brief description about this phenomenon is presented, and the corresponding experimental tools as well as the theoretical methods are introduced. Finally, the mechanism of this phenomenon is provided. At the end of Chapter 1, objectives and the accomplishments are given to provide guidelines about what we did in this work.

In Chapter 2, a literature review showing the previous work about surface segregation of Pt-based alloys and the ORR mechanism are provided. The literature review about surface segregation is focused on the theoretical study on the low-index surfaces of Pt-Ni, Pt-Co and Pt-Fe alloys system. Then we report some experimental results showing the advantages in the ORR catalytic activity of Pt-based alloys, followed by some theoretical study focused on the adsorption energy of species participating in ORR process on Pt and Pt-based alloys' surface. At the end of the chapter, the contribution of this work is provided.

Chapter 3 tells the story about surface segregation of Pt-Ni and Pt-Co alloys system. At first, we briefly describe the MEAM and MC simulation method applied in this work. Then computational details are provided in terms of three aspects: (1) Pt-Ni and Pt-Co potentials, (2) determination of lattice constants, and (3) examination of surface segregation. The results and discussion of the simulations are presented in the end.

Chapter 4 is about adsorption energy calculations. The methodology (DFT) and the detailed information of the computational model are provided at first. Adsorption energies of different ORR species and corresponding geometries are presented and discussed. Finally, conclusions and recommendation for future work are given in Chapter 5.

2. LITERATURE REVIEW

2.1 Surface Segregation for Pt-Ni, Pt-Co and Pt-Fe alloys

From the end of last century, experimental investigations of the surface segregation phenomena in binary alloy systems have been done by many groups. In Gauthier's work [8], surface-sandwich segregation at the (111) surfaces of disordered $Pt_{50}Ni_{50}$ and $Pt_{78}Ni_{22}$ alloys were observed by low-energy electron diffraction (LEED). For $Pt_{50}Ni_{50}$, the concentration in the first, second and third layers are 88 ± 2, 9 ± 5, and 65 ± 10 at.%, respectively. A nearly pure Pt top layer was found in $Pt_{78}Ni_{22}$ alloy with first layer containing 99 ± 1 at.% Pt. Two years later, his another paper [9] reported a segregation reversal on $Pt_{50}Ni_{50}$(110) surface. By LEED, enrichments of 100 at.% Ni, 95 at.% Pt, and 83 at.% Ni were measured in the first three layers.

In addition to Pt-Ni alloy, extended examination of concentration profiles on (111) surface of other Pt-based alloys have been done by Gauthier [10]. Results similar to Pt-Ni(111) were obtained by LEED for $Pt_{80}Fe_{20}$(111) and $Pt_{80}Co_{20}$(111) with Pt enriched outermost layers. The concentration profiles presented oscillation in Pt-Ni and Pt-Co alloys while monotonically decreased in Pt-Fe alloy.

Still done by Gauthier's group [11], the segregation at the reconstructed (1x2) missing row (110) surface of $Pt_{80}Fe_{20}$ disordered alloy was determined by LEED. It turned out that the top layer was enriched by Pt with an average concentration of 87% while the second layer containing 60% Pt which is less than the bulk concentration value of 80%.

It is difficult to theoretically predict surface segregation for Pt-based alloy system because it is sometimes orientation dependent and lack of reliable experimental technique to obtain the quantitatively reliable segregation energies. One technique that has been reported reliable is called photoemission spectroscopy of surface core-level shifts (SCLS) [12]. But it only feasible for very restricted set of dilute alloys. While for other alloys, estimation should be based on the Langmuir-McLean relation between bulk and surface composition, which is very sensitive to the environmental conditions and invalid if the ordering effects in the system cannot be neglected. For example, for Pt-Ni(110) surface, Langmuir-McLean relation predicted a Pt enriched surface while experiments showed a reverse segregation.

Abrikosov [13] did local-density calculations for three low-index surfaces at a specific concentration $Pt_{50}Ni_{50}$. Results showed that (111) and (100) surface were enriched by Pt, while the more open (110) surface was enriched by Ni. At the same concentration of 50%, Lundberg [14] and Stadler [15] both used embedded atom method (EAM) but got different results. Lundberg found Pt segregation on (110) surface, while Stadler reported a Ni segregated surface. Legrand [16] who applied semiempirical tight-binding ising model got results similar to Lundberg.

MC simulation combined with MEAM were used in Creemers' work [17] to obtain segregation profiles for $Pt_{50}Ni_{50}$(100), (110) and (111), and $Pt_{80}Fe_{20}$(111). It was found Pt atoms enriched on the (111) and (100) surfaces, whereas Ni atoms segregate to the (110) surface of $Pt_{50}Ni_{50}$ disordered alloys. Surface equilibrium concentrations of $Pt_{80}Fe_{20}$(111) were also obtained as a function of temperature. The results showed similar segregation as that of $Pt_{50}Ni_{50}$(111) surface, and the tendency of Pt segregation was a little bit weak at higher temperature.

Nilekar et al. [18] did a systematic test of surface energies for various bimetallic transition metal alloys. Focused on the low index (100) surface, the surface segregation energy for impurity Co atom in the host of Pt atoms was found to be 0.29 eV in this work,

which indicated Pt atoms would segregate to the outmost layer and Co may stay at the subsurface. The same conclusion was made for Pt-Fe alloy system with the segregation energy of 1.14 eV. However, the surface segregation energy for Ni atom was 0.00 eV, so which element will segregate to the surface cannot be judged by the surface segregation energy for Pt-Ni alloy system. In Ma's work [19], the surface segregation energies of (111) surface for a series Pt_3M alloy system were studied by DFT calculations. The results showed segregation energy of -0.61, -0.41 and -0.38 eV for Pt_3Co, Pt_3Fe and Pt_3Ni, respectively, which indicate Pt segregation in all three alloys. The more negative the energy, the stronger the tendency it shows.

2.2 ORR and Pt-based Alloys

Over the past two decades, Pt-based alloys have been investigated and discussed intensely in fuel cell field. Some 3-d metals alloyed with Pt catalysts have been reported to have a better performance for ORR than pure Pt. This was found both experimentally and theoretically.

Mukerjee at al. [20] found an increase of a factor of 2 to 3 in mass activity (mA/mg Pt at 0.9 V) when using Pt-Co or Pt-Ni compared to pure Pt, and Tamizhmani et al. [21] made a similar claim. Toda at al. [22] tested sputtered films of Pt-Co, Pt-Cr and Pt-Fe in 0.1 M $HClO_4$ at room temperature, which reflected an ORR activity enhancement regarding to pure Pt tested in the same experimental environment. U. A. Paulus et al. [23] reported a small activity enhancement for 25 at.% Ni and Co catalysts, and a more significant factor of 2 to 3 for the 50 at.% Co.

As a complement of experimental investigation, theoretical modeling has been applied to provide some detailed description of the ORR process at atomic or molecular level. The adsorption energy of ORR intermediates on the catalyst surface and the transition state calculations based on DFT are the most popular methods in this field.

Wang et al. [24] did Car-Parrinello molecular dynamics (CPMD) simulations on the electroreduction of O_2 on the Pt(111) surface and found out its rate determining step is the adsorption of H-O_2 species. Ford et al. [25] studied the adsorption of a group of atomic and molecular species on the Pt(111) surface through DFT-GGA calculations. The most stable adsorption sites and corresponding energies for each species at the coverage of 0.25 ML were determined. It was found that the atomic species are intended to be adsorbed at three-fold sites (for example, fcc site) and have higher binding ability than that of molecule species. In Hawkins' opinion [26], 0.25 ML is insufficient to fully investigate the initial oxidation, so he carried DFT calculations on the initial steps of oxidation at 0.25 and 0.5 ML on the Pt(111) surface. Also, he considered the subsurface oxidation. It was found in his work that at low coverage ($\leq$ 0.25 ML), the oxygen atoms was adsorbed to form a p(2x2) structure while it was dominated by p(2x1) structure when the coverage is larger than 0.5 ML. As for the Pt-based alloys, Xu et al. [27] studied the adsorption and dissociation of atomic and molecular oxygen on the ordered Pt_3Co and Pt_3Fe catalysts where the surfaces were covered by pure Pt skin through GGA-PW91 calculations. In addition to finding the adsorption configuration and energy, he also reported the relationship between oxygen dissociation and ORR activity as: the stronger the oxygen atom binds to the material, the easier for the molecule oxygen to dissociate to the surface, and hence improving ORR catalytic activity.

Hydroxyl chemisorption has been widely examined as the intermediate of water formation. Van Santen et al. [28] conducted a series DFT calculations using cluster model for the adsorption of OH on the surface of various 3-d and noble metals. It was found that the three-fold hollow sites are the favorite adsorption sites for OH on all the metals' surface and the corresponding chemisorption energies are between 1.8 and 3 eV. Same method used by Michaelides et al. [29] to examine the OH adsorption under different coverage on Pt(111) surface. They reported that OH prefer to be adsorbed at the bridge and top sites where the adsorption energies are about 2.25 eV at low coverage (from 1/9 to 1/3 ML). At the coverage of 1/2 to 1 ML, the top site is the energetic favorable adsorption site for OH with a 15% increase in the adsorption energy.

The adsorption of atomic oxygen on Pt(100) surface was investigated by Moussounda et al. [30] at different coverage from 0.25 to 1 ML. All calculations were carried out by DFT at GGA-PW 91 level. Several adsorption sites were examined and it turned out that the most stable site for atomic oxygen is the bridge site at all coverages. Similar work has been reported by Benesh and Liyanage [31] who also claimed that the bridge site is the most favored adsorption site for atomic oxygen on Pt(100) surface at the coverage of 0.5 ML.

A more comprehensive work were conducted by Oanchenko et al. [32], where the adsorption geometries and energies of atomic and molecular oxygen, H, OOH and H_2O_2 on the (111), (110) and (100) surface of Pt were investigated by periodic DFT. Oxygen molecule was revealed most stable when adsorbed at hollow and bridge positions at Pt (111) surface, whereas bridge sites for both (110) and (100) surfaces. The adsorption sites for atomic oxygen at Pt(111), (110) and (100) surface were three-fold hollow, bridge, and four-fold hollow, respectively. The top site is preferred for the adsorption of OH on Pt(111) and (110) surface, while the most stable adsorption site was turned to be bridge on the (100) surface.

Norskov [4] did an impressive work to explore the reason for the overpotential of ORR on the cathode in fuel cells. He claimed the ORR activity is in close relation with the adsorption energies of atomic oxygen and hydroxyl. It turned out that Pt and Pd are the best pure metal catalysts for ORR, but there is still some space for improvement by finding a catalyst with weaker atomic oxygen and hydroxyl binding ability. This research provided a clue on how to design a better cathode catalyst for fuel cells.

2.3 Contribution of This Work

In this work, we developed MEAM potentials for Pt-Ni and Pt-Co alloys to correctly predict surface segregation phenomenon. Pt-Ni alloys exhibit surface orientation-dependent segregation in which the driving forces are in close competition with each other, thus it is difficult to theoretically describe the surface segregation

phenomena. Instead of predicting concentration profiles for single surface, our work reproduces the concentration profile for three different surfaces: (111), (110) and (110) (1x2) missing row surfaces. Compared to previous works done by others who only did modeling on one or two specific concentrations, our work built the concentration profiles as a function of bulk Pt concentration from 5 at.% to 95 at.% with linear increase of 5 at.%.

In the second part, adsorption of four species (O, O_2, H_2O, OH) participating in ORR process were investigated by spin polarized DFT. Two low-index surfaces: (111) and (100) of Pt-Co, Pt-Ni and Pt-Fe alloys and various high-symmetry adsorption sites were taken into consideration. Moreover, we introduced surface segregation based on our MC simulations into the surface slab models, to study ORR more close to real situation.

3. SURFACE SEGREGATION OF DISORDERED PT-NI AND PT-CO ALLOYS

3.1 Methodology

3.1.1 MC Simulation Method

MC simulation method proves advantageous in modeling the surface segregation phenomena of multi-component alloys. This mainly because that the MC simulation is able to avoid slow physical dynamic processes (such as diffusion) in the material system and provide an averaged composition profile over a thermodynamic equilibrium ensemble. Consequently, we employed the MC simulation method in this work to drive the equilibrium composition of the (111) and (110) surfaces of Pt-Ni alloys, and (111) surface of Pt-Co alloys at finite temperature. In our simulation, we applied a canonical ensemble statistical mechanics. That is the total number of atoms of each element and the simulation temperature are kept constant. Starting from some atomic configuration, a series of configuration transformations are performed to reach the thermodynamically equilibrated states of the simulated system. In the equilibrium stage of our MC simulations, the configurations will be generated in proportion to the probability of a configuration occurring in the equilibrium ensemble.

Specifically, one of the following two configuration changes is attempted with an equal probability in each MC simulation step:

1) randomly selected atom is displaced from its original position. This operation accounts for the positional relaxation process.
2) randomly selected atoms with different element types are exchanged. This operation accounts for the compositional relaxation process.

The energy change ΔE between the new and old configurations after each configuration change was then calculated. If the energy decreases ($\Delta E < 0$), we always keep the new configuration; while the energy increases ($\Delta E > 0$), the new configuration is retained with a probability P given by Eq. 3.1,

$$P = \exp(-\frac{\Delta E}{k_B T}) \qquad \text{Eq. 3.1}$$

where k_B is the Boltzmann constant and T is the temperature.

3.1.2 MEAM

In order to accurately evaluate the energy change ΔE of the configuration transformation, we used MEAM to describe the atomic interaction potentials of Pt-Ni alloys. In EAM, the electron density is only atomic separation dependent. Improved from original EAM potentials, MEAM potentials take many-body effect, angular dependent terms, and nearest-neighbor contribution into considerations. Detailed description about MEAM can be found in the literature [33 - 34]. Here we only give a brief introduction about MEAM.

The total energy of a system in MEAM can be expressed by Eq. 3.2,

$$\mathrm{E}=\sum_i \left[F\left(\bar{\rho}_i\right) + \frac{1}{2}\sum_{j\neq i} \Phi\left(R_{ij}\right) \right] \qquad \text{Eq. 3.2}$$

where $\bar{\rho}_i$ is the background electron density at the center of atom i calculated by superposition of electronic densities from its surrounding atoms; $F\left(\bar{\rho}_i\right)$ is the embedding energy for atom i which is embedded into the background electron density $\bar{\rho}_i$, and $\Phi\left(R_{ij}\right)$ is the core-core pair repulse between atom i and j with an inter-atomic distance R_{ij}.

The embedding energy can be further described as follows.

$$F(\bar{\rho}) = AE_c\left(\frac{\bar{\rho}}{\bar{\rho}^0}\right)\ln\left(\frac{\bar{\rho}}{\bar{\rho}^0}\right) \qquad \text{Eq. 3.3}$$

Here, A is an adjustable parameter, E_c donates the cohesive energy, and $\bar{\rho}^0$ is the density scaling parameter.

The spherically symmetric partial electron density $\bar{\rho}_i$ and three angular partial electron densities $\rho_i^{(1)}$, $\rho_i^{(2)}$ and $\rho_i^{(3)}$ have contributions to the electron density $\bar{\rho}_i$. These partial electron densities are shown as below.

$$\rho_i^{(0)} = \sum_{j(\neq i)} \rho_j^{a(0)}(R_{ij}) \qquad \text{Eq. 3.4}$$

$$(\rho_i^{(1)})^2 = \sum_{\alpha}\left[\sum_{j(\neq i)} x_{ij}^{\alpha}\rho_j^{a(1)}(R_{ij})\right]^2 \qquad \text{Eq. 3.5}$$

$$(\rho_i^{(2)})^2 = \sum_{\alpha,\beta}\left[\sum_{j(\neq i)} x_{ij}^{\alpha}x_{ij}^{\beta}\rho_j^{a(2)}(R_{ij})\right]^2 - \frac{1}{3}\left[\sum_{j(\neq i)}\rho_j^{a(2)}(R_{ij})\right]^2 \qquad \text{Eq. 3.6}$$

$$(\rho_i^{(3)})^2 = \sum_{\alpha,\beta,\gamma}\left[\sum_{j(\neq i)} x_{ij}^{\alpha}x_{ij}^{\beta}x_{ij}^{\gamma}\rho_j^{a(3)}(R_{ij})\right]^2 - \frac{3}{5}\sum_{\alpha}\left[\sum_{j(\neq i)} x_{ij}^{\alpha}\rho_j^{a(3)}(R_{ij})\right]^2 \qquad \text{Eq. 3.7}$$

Here $x_{ij}^{\alpha} = R_{ij}^{\alpha}/R_{ij}$. R_{ij}^{α} is the α component (α = x, y, or z) of the distance vector between atoms i and j. $\rho_j^{a(h)}(R_{ij}) = e^{-\beta^{(h)}(R_{ij}/r_e - 1)}$ (h = 0, 1, 2 and 3 is the electron density for atom i contributed from atom j, r_e is the nearest-neighbor distance according to the equilibrium lattice constants.

Equation 3.8 and 3.9 are the formula to calculate the background electron density.

$$\bar{\rho}_i = \rho_i^{(0)}\sqrt{1+\Gamma_i} \qquad \text{Eq. 3.8}$$

$$\Gamma_i = \sum_{h=1}^{3} t^{(h)}\left[\rho_i^{(h)}/\rho_i^{(0)}\right]^2 \qquad \text{Eq. 3.9}$$

where $t^{(h)}$ are adjustable parameters.

The core-core pair repulsion is given as follows.

$$\Phi(R) = \frac{2}{Z}\left\{E^u(R) - F[\rho^0(R)]\right\} \quad \text{Eq. 3.10}$$

Here, Z is the number of nearest neighbors in the bulk structure; E^u is the energy per atom of the reference structure, which is computed by the following equations [35],

$$E^u(R) = -E_c(1+a^*)e^{-a^*} \quad \text{Eq. 3.11}$$

$$a^* = \alpha(R/r_e - 1) \quad \text{Eq. 3.12}$$

$$\alpha = \sqrt{\frac{9\Omega B}{E_c}} \quad \text{Eq. 3.13}$$

where E_c is the cohesive energy, r_e is the nearest-neighbor distance, Ω is the atomic volume and B is the bulk modulus of the equilibrium reference structure.

In Eq. 3.10, $\rho^0(R)$ donates the background electron density for the equilibrium reference structure. Different formulas are employed to calculate $\rho^0(R)$ for fcc metals and hcp metals. For fcc metals,

$$\bar{\rho}^0(R) = Z\rho^{a(0)}(R) \quad \text{Eq. 3.14.}$$

While for hcp metals,

$$\bar{\rho}^0(R) = Z\rho^{a(0)}(R)\sqrt{1+\frac{t^{(3)}}{3Z^2}\left(\frac{\rho^{a(3)}}{\rho^{a(0)}}\right)^2} \quad \text{Eq. 3.15.}$$

Many-body screening function is used to determine the nearest neighbors of an atom. Proposed by Baskes [36], elliptical construction is applied to complete the screening procedure. The screening function S_{ik} between atoms i and j can be described as Eq. 3.16.

$$S_{ik} = \prod_{j \neq i,k} S_{ijk} \quad \text{Eq. 3.16}$$

It indicates the screening function of certain atom depends on all the atoms between them. And,

$$S_{ijk} = f_c\left(\frac{C - C_{\min}}{C_{\max} - C_{\min}}\right) \qquad \text{Eq. 3.17}$$

where f_c is a cutoff function of C_{max} and C_{min} which are material dependent parameters. C is computed by:

$$C = \frac{2(X_{ij} + X_{jk}) - (X_{ij} - X_{jk})^2 - 1}{1 - (X_{ij} - X_{jk})^2} \qquad \text{Eq. 3.18}$$

where $X_{ij} = (r_{ij}/r_{ik})^2$ and $X_{jk} = (r_{jk}/r_{ik})^2$, in which r_{ij}, r_{jk} and r_{ik} are the atomic distance between the corresponding atoms.

The cutoff function f_c has forms as described in Eq. 3.19 - 3.21, depending on the range of x.

If $x \geq 1$, $f_c(x) = 1$ Eq. 3.19

If $0 < x < 1$, $f_c(x) = \left[1 - (1-x)^4\right]^2$ Eq. 3.20

If $x \leq 0$, $f_c(x) = 0$ Eq. 3.21

3.2 Computational Details

3.2.1 Pt-Ni and Pt-Co potentials

The potentials used in MEAM for Pt, Ni and Co were previously developed using empirical data for the lattice constants, cohesive energy, elastic constants and vacancy formation energy. Table 3.1 and 3.2 list the fitting parameters for the MEAM potentials of Pt, Ni and Co. These parameters are the cohesive energy E_c (eV), the equilibrium nearest-neighbor distance r_e (Å), the exponential decay factor for the universal energy

function α, the scaling factor for the embedding energy A, the four exponential decay factors for the atomic densities $\beta^{(i)}$, the four weighting factors for the atomic densities $t^{(i)}$, and the density scaling factor ρ^0.

Table 3.1 Fitting parameters for MEAM potentials of Pt, Ni and Pt-Ni

	E_c	r_e	α	A	$\beta^{(0)}$	$\beta^{(1)}$	$\beta^{(2)}$	$\beta^{(3)}$	$t^{(0)}$	$t^{(1)}$	$t^{(2)}$	$t^{(3)}$	ρ^0
Ni	4.45	2.49	4.99	1.10	2.45	1.50	6.00	1.50	1.00	5.79	1.60	3.70	1.00
Pt	5.77	2.77	6.44	1.04	4.67	2.20	6.00	2.20	1.00	4.70	-1.38	3.29	1.10
Pt-Ni	5.52	2.70	6.43										

Table 3.2 Fitting parameters for MEAM potentials of Pt, Co and Pt-Co

	E_c	r_e	α	A	$\beta^{(0)}$	$\beta^{(1)}$	$\beta^{(2)}$	$\beta^{(3)}$	$t^{(0)}$	$t^{(1)}$	$t^{(2)}$	$t^{(3)}$	ρ^0
Co	4.41	2.50	5.12	1.05	2.10	0.00	6.00	2.20	1.00	9.00	-1.00	-1.00	1.19
Pt	5.77	2.77	6.44	1.04	4.67	2.20	6.00	2.20	1.00	4.70	-1.38	3.29	1.26
Pt-Co	5.50	2.72	6.29										

Table 3.3 Angular screening parameters for MEAM potentials of Pt-Ni

	Pt-Pt-Pt	Pt-Ni-Pt	Ni-Pt-Pt	Ni-Ni-Pt	Ni-Pt-Ni	Ni-Ni-Ni
C_{max}	2.80	2.80	2.80	2.80	2.80	2.80
C_{min}	0.80	2.00	1.00	1.00	0.80	0.80

Table 3.4 Angular screening parameters for MEAM potentials of Pt-Co

	Pt-Pt-Pt	Pt-Co-Pt	Co-Pt-Pt	Co-Co-Pt	Co-Pt-Co	Co-Co-Co
C_{max}	3.06	2.11	4.00	2.23	3.60	4.00
C_{min}	1.37	1.01	1.30	1.02	1.50	0.80

Table 3.3 and 3.4 show the angular screening parameters for Pt-Ni and Pt-Co alloy potentials, respectively. Details about angular screening function were described in reference [37]

3.2.2 Determination of Lattice Constants

First, we applied the MC simulation method to determine the lattice constants of disordered Pt-Ni bimetallic alloys at the temperature of T = 1000 K, 1200 K, 1400 K, respectively. To this end, we modeled the Pt-Ni bulk alloy using a cubic cell containing 500 atoms, with face-centered cubic (fcc) lattice structure, and with three dimensional periodic boundaries. Initially, we randomly distributed the Pt and Ni atoms in the fcc lattice sites of the modeled simulation cells according to the composition of Pt-Ni alloys. Starting from that constructed structure, we then performed 2×10^6 steps of MC simulations considering both compositional and structural relaxation processes to reach the thermodynamic states of the disorder Pt-Ni alloys at the specific temperature. During the MC simulation, the cell pressure was evaluated at every 1000 MC steps. Eliminating the influence of the initial structure on final results, we calculated the average pressure of the simulation cells only for the last 1×10^6 MC steps in this work. The equilibrium lattice parameter of the Pt-Ni alloy is the one that leads to zero average pressure at its thermodynamic states. Consequently, for each given composition of Pt-Ni alloys, we conducted a similar MC simulation for the simulation cells with various lattice parameters and found the simulation cell in which the computed average pressure is nearly zero. Moreover, we adjusted the magnitude of the maximum atomic displace for our MC simulations so that the acceptance rate of new configuration due to displacement of atoms is about 0.5 during the equilibrated part of the simulations. This better ensures the convergence of our MC simulations for the bulk Pt-Ni alloys with different compositions. A flow chat summarizing the whole process can been seen in Figure 3.1

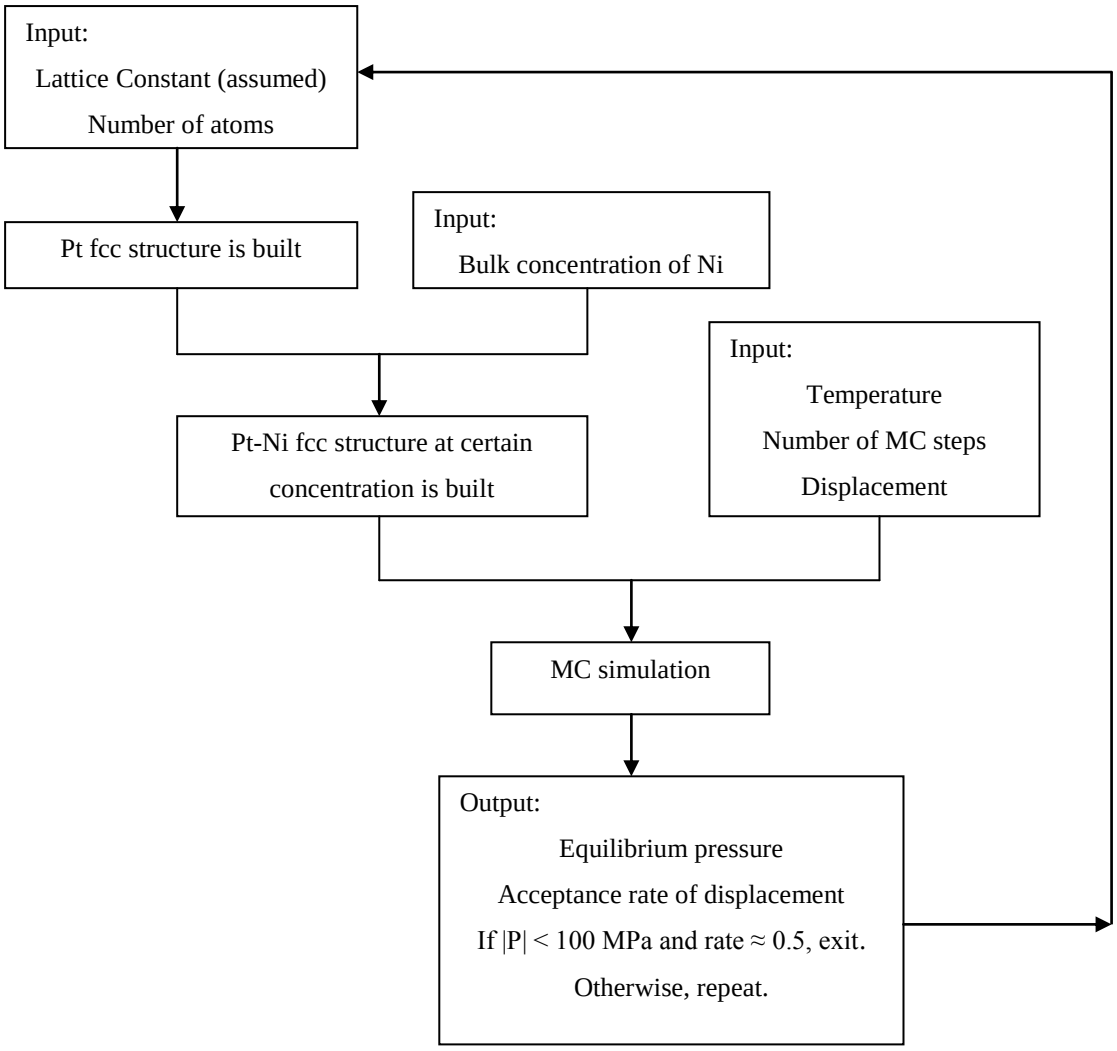

Figure 3.1 Steps of lattice parameter calculations

3.2.3 Examination of Surface Segregation

We applied our MC simulation method to simulating the (111) surfaces of Pt_xNi_{100-x} alloys using slab models and determining the equilibrium composition of each individual surface layers. Our slab models for the (111) surfaces of Pt_xNi_{100-x} alloys were constructed as follows. The three orthogonal axes of the simulation cell are along $[1\bar{1}0]$, $[11\bar{2}]$, and [111] directions; periodic boundary condition is applied to the boundaries normal to the $[1\bar{1}0]$ and $[11\bar{2}]$ directions but free boundary condition to the boundary normal to the [111] direction; and an fcc lattice containing 15 layers in the [111] direction

and 36 atoms in each layer is built with randomly distributed Pt and Ni atoms and a lattice parameter determined from the MC simulation in Section 4.3.1. Thus, there are two (111) surfaces whose outermost layers are separated by about 30 Å in our model. For the equilibrium composition of each surface layer, we calculate the average of the values from those two surfaces.

In the initial slab model for the (111) surfaces of Pt_xNi_{100-x} alloys, the Pt and Ni atoms are distributed randomly so that the composition of each surface layer is the same as the overall composition of the alloy. In addition, the initial separations between neighboring (111) surface layers are set to be those values determined by the lattice parameter of the bulk Pt-Ni alloy. From these configurations of (111) surface models, we performed MC simulations including the exchange of different elements and the displacement of atoms in the [111] direction for 10×10^6 steps at T = 1200 K. Exchange of different elements enables a proper evolution of the composition in the surface region, while displacement of atoms in the [111] direction (the maximum displacement of atoms is 0.02 Å at each MC step) allows a reasonable adjustment of the inter-layer distances of (111) surfaces. The Pt and Ni atoms differ by about 10 % in their atomic sizes; hence a correct separation between the surface layers is an essential factor in simulating the surface segregation process for the extended surfaces of Pt-Ni alloys. There are only 540 atoms in our slab models of the (111) surface in this work and this finite size of our model constricts how many atoms would segregate to the surfaces. In contrast, there is sufficient supply of the segregating atoms in the experimental sample of extended (111) surfaces. Consequently, the extent of surface segregation might be underestimated if we conducted the MC simulation using the slab models to have exactly the same overall composition as the bulk crystal with the same lattice parameter. To correct this deficiency, we have done a series of MC simulations for each extended surface slab of Pt-Ni alloys with different overall compositions, and determined the surface composition profiles from the simulation that leads to the desired bulk composition in the center of the slab.

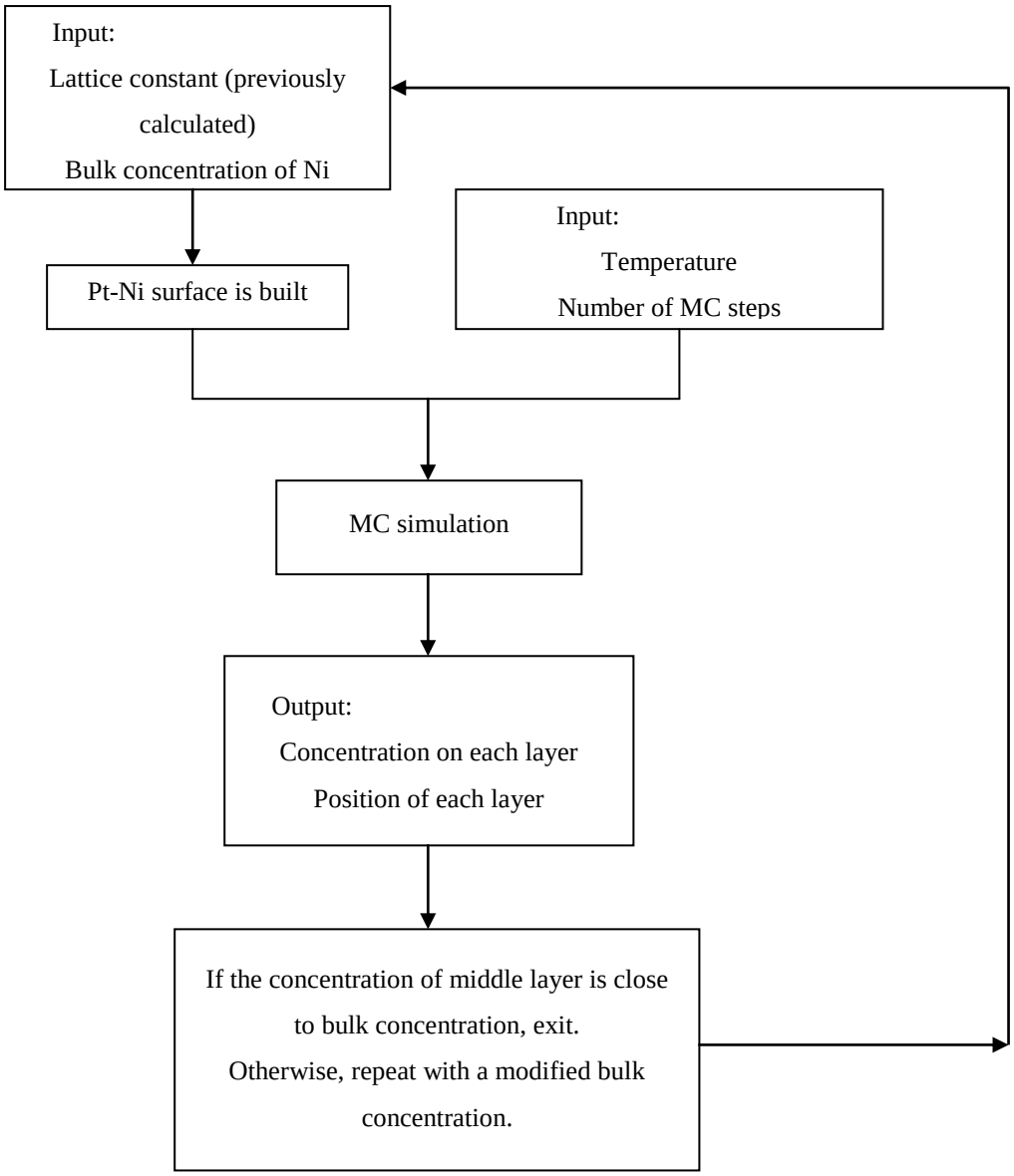

Figure 3.2 Steps of surface segregation modeling

After about 2 million steps, the total energy of the simulated (111) surface slabs have already converged in our MC simulations. We computed the equilibrium compositions of the three outermost surface layers by averaging the corresponding concentrations of Pt every 1000 MC steps in the last 5 x 10^6 steps. Figure 3.2 shows the procedure of surface segregation modeling.

For Pt-Co alloys, the whole procedure is the same as we did for Pt-Ni alloys. At temperature 1200 K, we first obtained equilibrium lattice parameters as a function of bulk Pt concentration and then applied MC simulation method to build the (111) surface segregation profile.

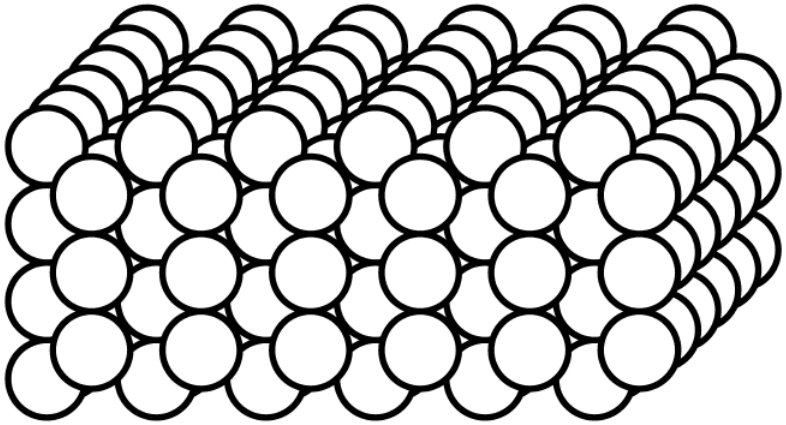

(a) unreconstructed (110) surface

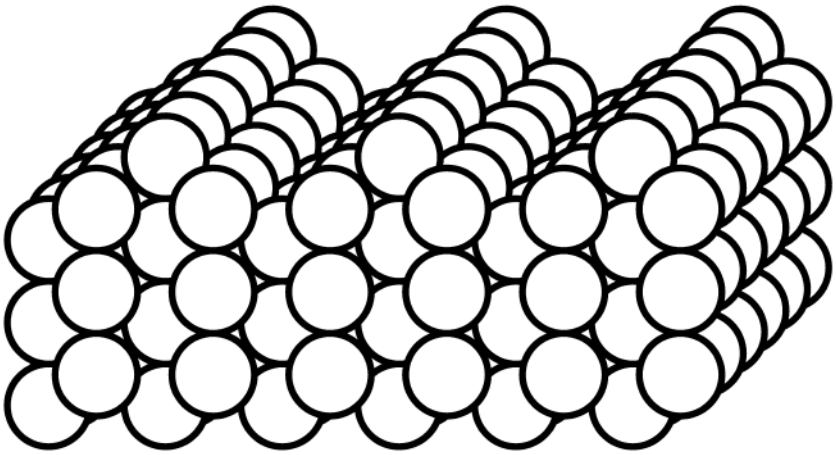

(b) (1x2) missing row reconstructed (110) surface

Figure 3.3 (a) and (b) Top view of (110) surface.

Similarly, we conducted MC simulation on unreconstructed and reconstructed (110) surface. Remarkable reconstruction can be found on some metals' surface due to

the force which cause surface relaxation and lead to a change in the equilibrium position and bonding of surface atoms. Most of semiconductors (Si, Ge, In, Sb, etc.) have their surface reconstructed. The Pt-Ni (110) surface that is discussed here also presents a so-called "missing-row" reconstruction. In this configuration, a whole row of metal atoms is missing periodically, which gives rise to a (1x2) surface structure.

Figure 3.3 shows the top view of the structure of surface (110). For surface (110), slab simulation cells containing 1140 atoms were employed, where the number of atoms in the outermost layer on one side was 48. Relaxation is of extremely importance to obtain the correct surface segregation result for (110) surface, due to the structural instability of (110) surface in fcc crystals. Thus, interlayer distance relaxation is included in each MC simulation step. We took 10 million steps MC simulation for both unreconstructed and reconstructed (110) surface and eliminated the results of the first 5 million steps in order to get rid of the effect of initial structures. The final result was sampled every 1000 steps of the last 5 million steps. To further test our MC simulation model, we performed the same process for reconstructed (110) surface at 1000 K and 1400 K.

3.3 Results and Discussion

3.3.1 Lattice Constant Profile

In Figure 3.4 and 3.5, we plotted the lattice parameters obtained from our MC simulations for disordered Pt_xNi_{100-x} and Pt_xCo_{100-x} alloys at T = 1200 K, respectively. In the plots, the theoretical data from this work are represented with the circles. For comparison, the experimental data [38] are plotted with the solid up-triangles. It is seen in both figures that the calculated lattice parameters increase proportionally linearly with the increase of the Pt concentration of these two alloys. This is well consistent with empirical Vegard's law which states that the lattice parameter should be in an approximate linear relation with the composition of a solid solution containing two constitutes. It notes that

in the experimental measurements the alloys were annealed at 1100 °C (1373 K) for 10 days and quenched to attain the disordered solid solutions for Pt-Ni alloys. While the Pt-Co alloys were prepared by melting Pt and Co under carbon monoxide and then casting. After cold-worked and homogenized at 1000 °C (1273 K) to 1100 °C (1373 K) for a whole day, the lattice spacings were determined by quenching the alloys from 850 ^{o}C (1123 K) or a higher temperature. Shown in Figure 3.4 and 3.5, our theoretical results are in excellent agreement with experimental data: the difference between theory and experiment is less than 5 %. These results indicate that our MEAM potential and MC simulation method are capable of accurately describing the atomic size effect in Pt_xNi_{100-x} and Pt_xCo_{100-x} alloys.

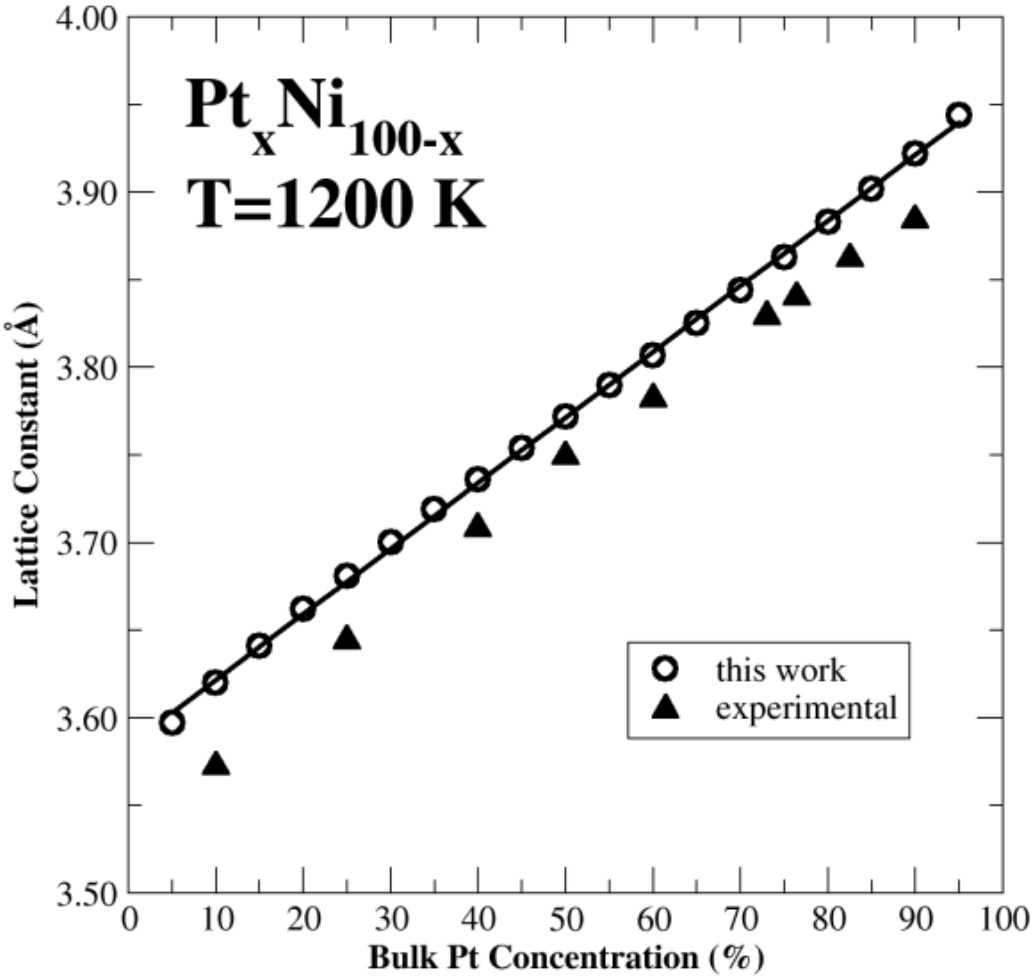

Figure 3.4 Lattice parameters for Pt_xNi_{100-x} alloys at 1200 K

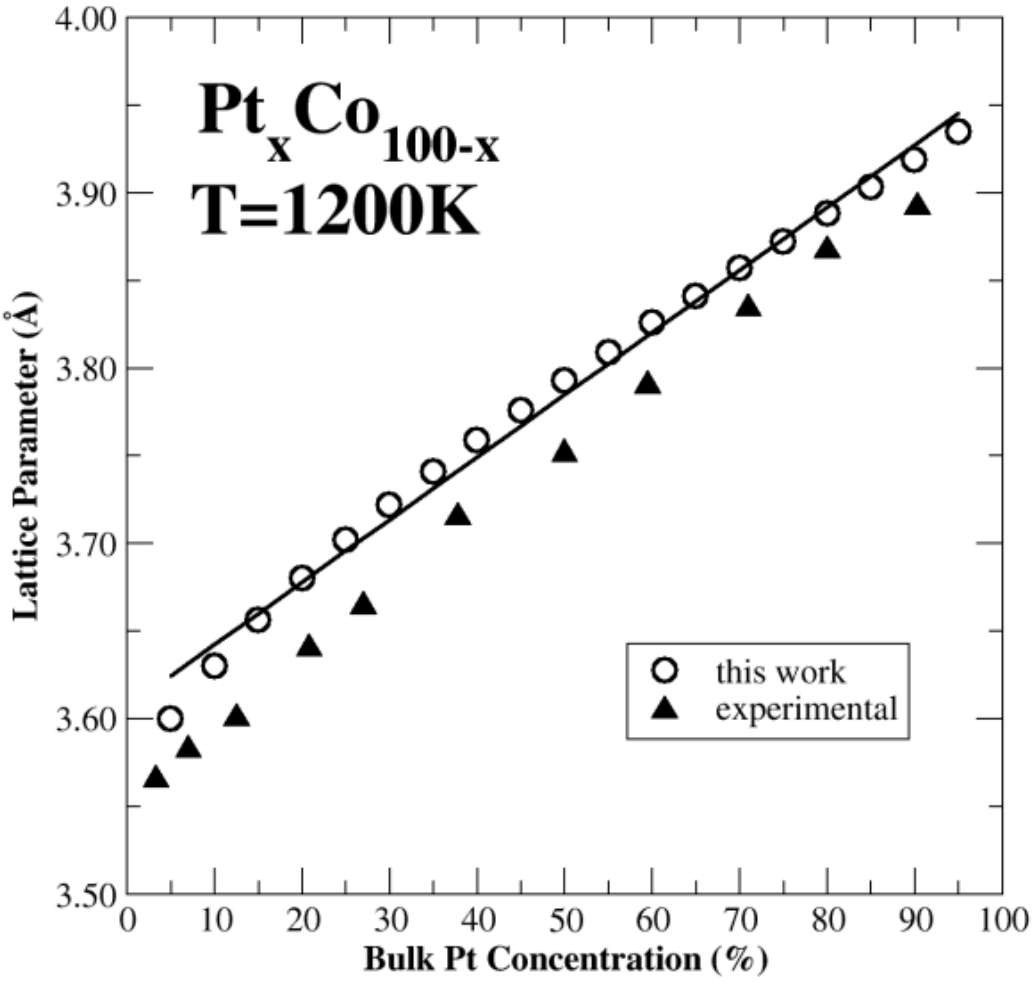

Figure 3.5 Lattice parameters for Pt_xCo_{100-x} alloys at 1200 K

We conducted MC simulations to calculate lattice constants for disordered Pt-Ni alloys system at three different temperatures to further test the reliability of our model. Figure 3.6 gives out the results of these simulations. The rectangles represent the lattice parameters at the temperature of 1000 K; data for 1200 K are plotted with circles; the down-triangles show the results at temperature of 1400 K. For comparison, we also put experimental data in solid filled up-triangles in this picture. We can see that the lattice constants increase along with the raise of the temperature showing thermal expansion for Pt-Ni alloys. Similar as that of 1200 K, the data points obtained at temperature of 1000 K and 1400 K both exhibit a linear tendency with respect to the bulk Pt concentration. The

value of parameters calculated by our model fit well with the experimental data, especially at temperature of 1400 K.

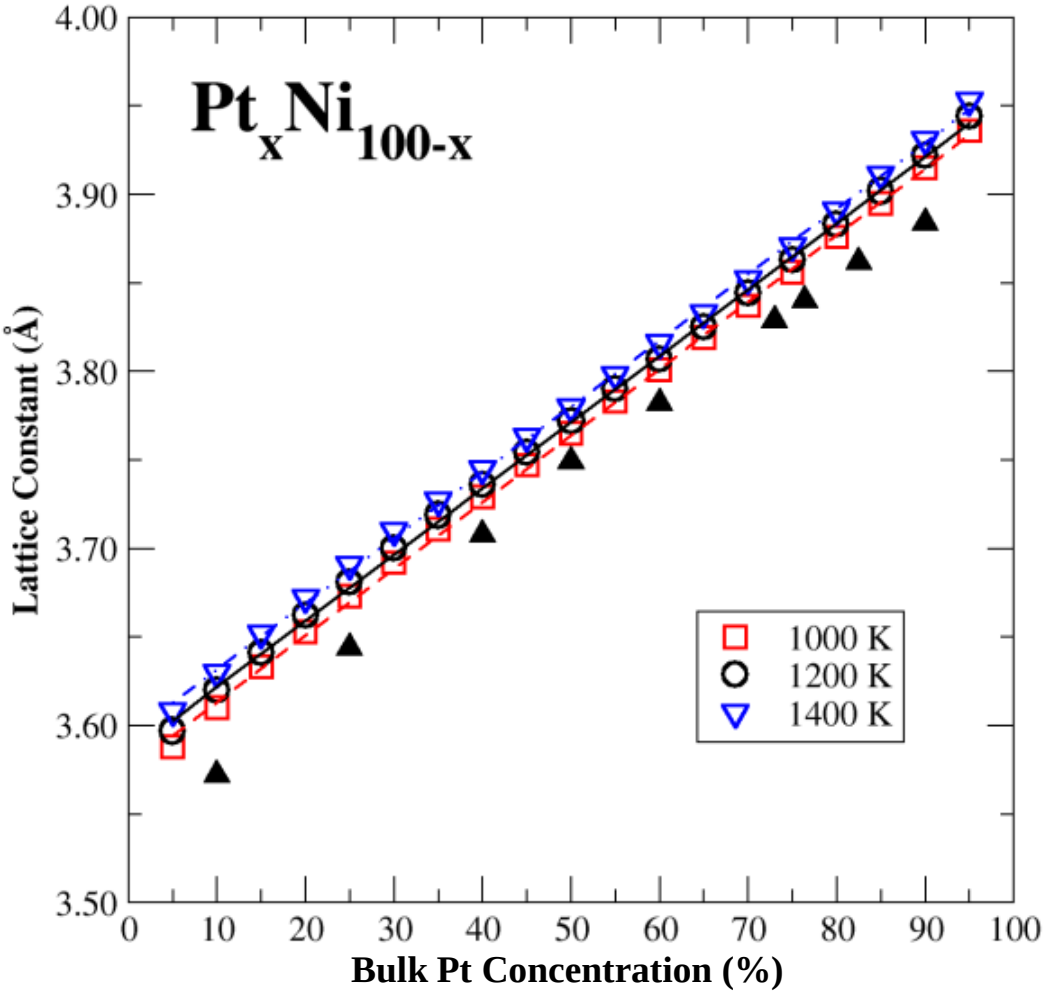

Figure 3.6 Comparison of lattice parameters of Pt_xNi_{100-x} alloys system at 1000 K, 1200 K and 1400 K

3.3.2 Surface Segregation

3.3.2.1 Pt-Ni and Pt-Co alloys (111) surface segregation at 1200 K

Figure 3.7 plots the calculated Pt concentrations in the outermost three layers of (111) extended surfaces as a function of the bulk composition of Pt_xNi_{100-x} alloys. The temperature of the MC simulations is 1200 K. Symbols (circles, squares, and diamonds) represent the theoretical data from MC simulations. The solid lines are the polynomial function fitting to those data and used to guide the eye. The dashed line indicates where the surface Pt concentration equals the bulk value.

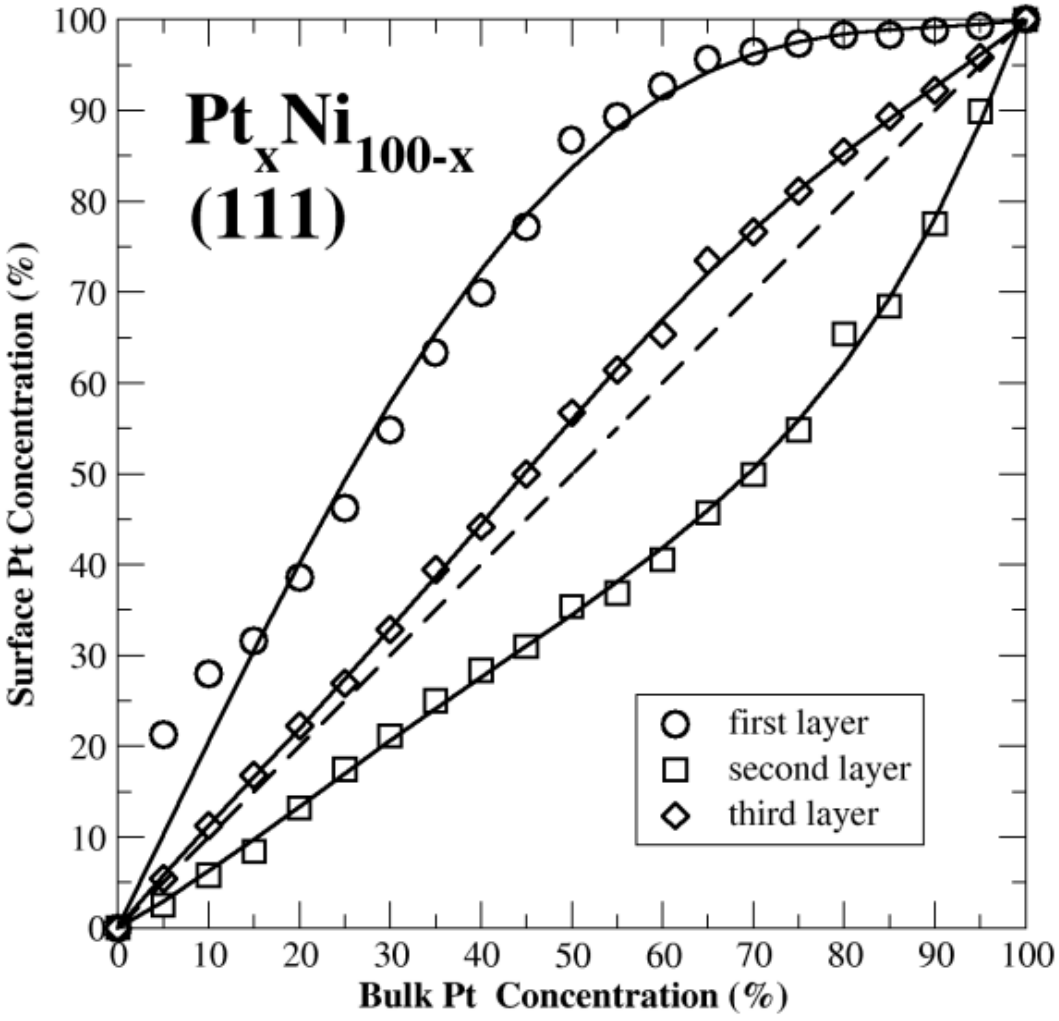

Figure 3.7 Surface concentrations versus bulk concentrations of Pt for Pt_xNi_{100-x}(111) surface at T = 1200K

The results show a strong segregation of Pt to the outermost layer and Ni to the second sub-layer. Moreover, we give in Table 3.5 a quantitative comparison between our theoretical results and experimental data. The agreement between theory and experiment is remarkable. This result evidences that our MEAM potential and MC simulation method are capable of accurately describing the surface segregation phenomena in Pt_xNi_{100-x} alloys.

Table 3.5 Comparison of the Pt concentrations on the outermost three layers of the (111) surface for $Pt_{10}Ni_{90}$, $Pt_{50}Ni_{50}$, and $Pt_{78}Ni_{22}$ alloys between MC simulations at T = 1200 K and experiment measurements.

	Layer 1	Layer2	Layer3
$Pt_{10}Ni_{90}$			
MC simulation	28	6	11
Experiment [39]	30	5	
$Pt_{50}Ni_{50}$			
MC simulation	87	35	57
Experiment [8]	88	9	65
$Pt_{78}Ni_{22}$			
MC simulation	98	56	83
Experiment [8]	99	30	87

Figure 3.8 shows the Pt concentrations at the first, second and third layer of the close-packed (111) surfaces with respect to the bulk composition of Pt_xCo_{100-x} alloys. The segregation simulation carried out at temperature of 1200 K, under which the Pt_xCo_{100-x} alloys are in disordered state. Circles, squares and diamonds are theoretical data points obtained by MC simulations. Polynomial function curve fitting of these data points are shown by solid lines. The dashed line presents the surface concentration of Pt equals to the bulk value.

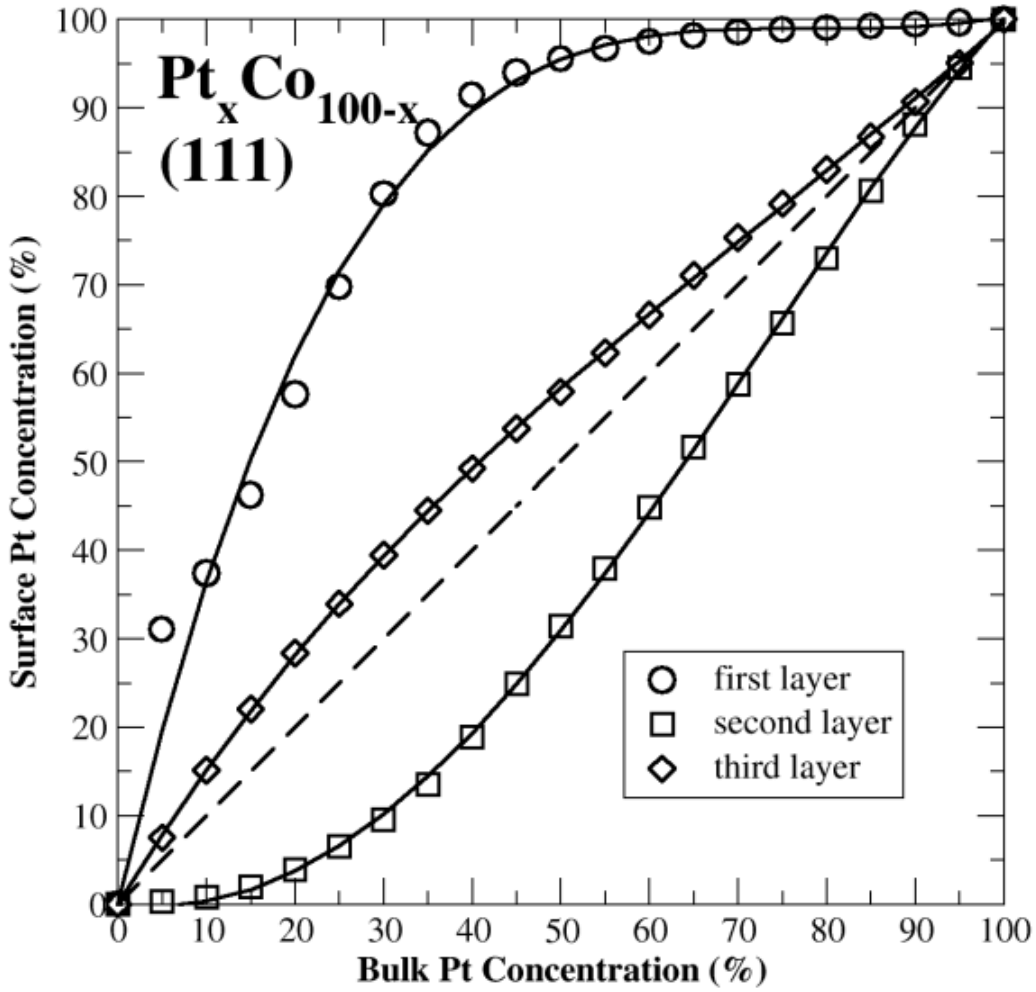

Figure 3.8 Surface concentrations versus bulk concentrations of Pt for Pt_xCo_{100-x} (111) surface at T = 1200 K

As can be seen in Figure 3.7, Pt atoms segregate to the outmost and third layers, while Co atoms enrich in the second layer. We notice that, compared with Pt_xNi_{100-x} alloys, Pt atoms have stronger tendency to segregate to the first layer in the Pt_xCo_{100-x} alloys at low bulk Pt concentration. For comparison, Table 3.6 gives some experimental data for $Pt_{25}Co_{75}$ and $Pt_{80}Co_{20}$. Though the value obtained by MC simulation may not fit well with that from experiments, the segregation tendency keeps correspondence with the experiments. As mentioned before, at low Pt bulk concentration, say $Pt_{25}Co_{75}$, the Pt concentration on layer 1 is higher than in $Pt_{25}Ni_{75}$. This phenomenon can also be

observed in experiments. We also noticed that at high concentration, say above 80 at.% Pt, the concentration of Pt atoms at the second layer excess that of the bulk concentration, which is different from Pt_xNi_{100-x} alloys. Since no experiment has been done at the higher concentration than 80 at.% Pt, it is hard to tell whether such kind of phenomenon would occur in reality. Otherwise, we can further adjust the MEAM potential for Pt-Co to make the prediction more accurate when compared to the results obtained by experiments and improve the reliability for the cases with higher Pt bulk concentrations.

Table 3.6 Comparison of the Pt concentrations in the outermost three layers of the (111) surface for $Pt_{25}Co_{75}$, $Pt_{50}Co_{50}$, and $Pt_{80}Co_{20}$ alloys between MC simulations at T = 1200 K and experimental measurements.

	Layer 1	Layer2	Layer3
$Pt_{25}Co_{75}$			
MC simulation	64	1	40
Experiment [40]	46.8	2.9	25
$Pt_{80}Co_{20}$			
MC simulation	99	74	83
Experiment [10]	99.4	50	87

Normally, element with lower surface energy will segregate to the surface. For Pt_xCo_{100-x} alloys, Pt atoms segregate to the outmost layer to lower the system's surface energy because they have less surface energy than that of Co atoms. Since the surface energy of Ni is only slightly less than that of Pt, the surface segregation of (111) surface cannot be explained only by surface energy factor. The physics origins for this observed segregation phenomenon are: (a) Pt atoms are larger than Ni atoms in fcc crystal lattices, thus segregating Pt atoms to the outermost surface layer of the close-packed (111) surfaces of Pt-Ni alloys would reduce the total strain energy of the surface slabs; and (b) the bonding between Pt and Ni atoms are stronger than the ones of Pt-Pt or Ni-Ni, consequently segregating Ni atoms to the second layer of the (111) surface after Pt atoms

to the outermost layer would maximize the total number of Pt-Ni bonds and hence decrease the total energy of the surface slabs. Our MEAM potentials and MC simulations captured those material physics mechanisms and predicted a correct segregation fashion for the (111) surfaces of Pt-Ni alloys.

3.3.2.2 Pt-Ni alloys (110) Surface Segregation at 1200 K

As shown in Figure 3.9, with a different "surface - sandwich structure" compared with (111) surface, this time, Ni atoms segregate to the outermost and third atomic layer while Pt atoms segregate to the subsurface.

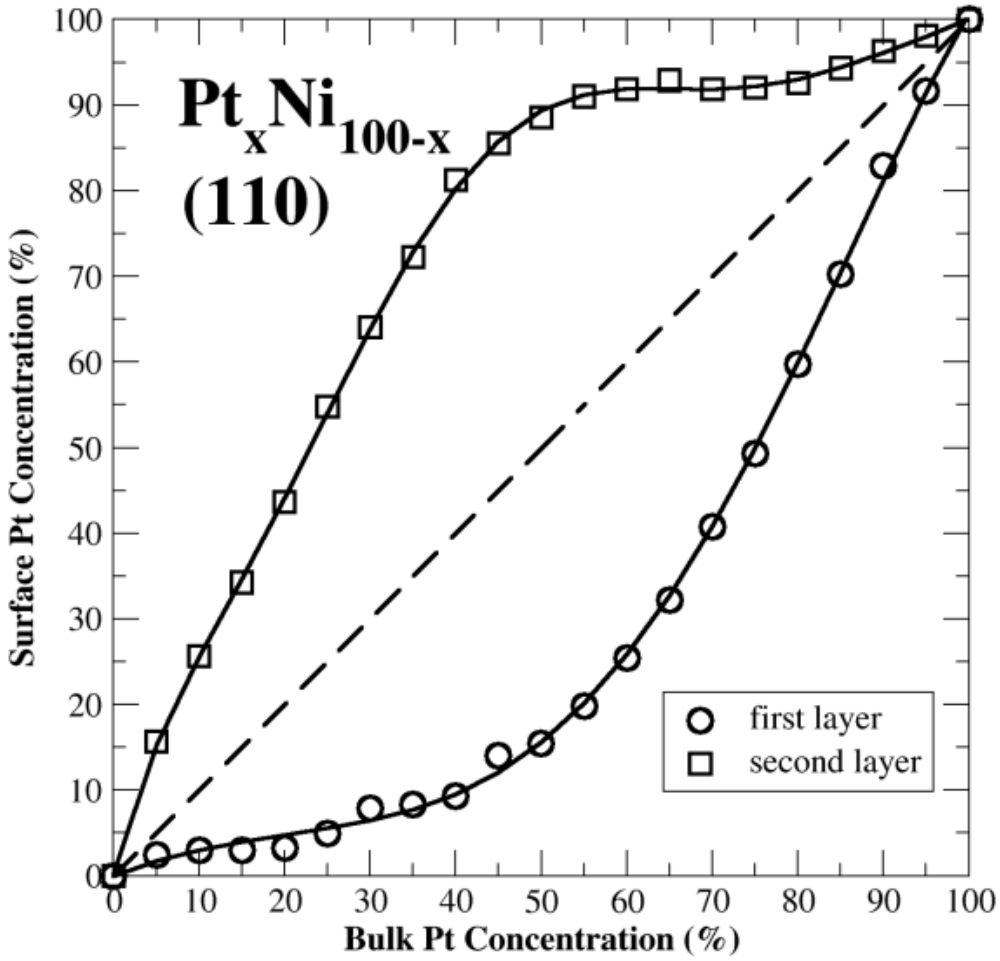

Figure 3.9 Surface concentrations versus bulk concentrations of Pt for Pt_xNi_{100-x} (110) surface at T = 1200 K

For the more rough (110) surface, the segregation phenomenon seems dominated by the difference of surface energy for Ni atoms enrich on the first layer. Other explanation is that the Pt atoms have the tendency to segregate both to the outmost layer and subsurface, while the tendency to enrich the subsurface is stronger. Pointed out by Abrikosov [13], for the more open (110) surface, the interlayer distance is small and coordination number of the atoms in the subsurface is less than the bulk value, which promote Pt atoms to segregate to the second layer.

3.3.2.3 Pt-Ni Alloys (110) (1x2) Missing Row Surface Segregation

First, we obtained the segregation profile at the temperature of 1200 K. In Figure 3.10 (a), it is interesting to find out that the surface segregation condition has a 180 degree change for the (110) surface with missing row compared with unreconstructed (110) surface. We can see that Pt atoms segregate to the outermost atomic shell again, which is similar as that of (111) surface. But for high bulk Pt concentration (from 80 at.% to 95 at.%), more Pt atoms enrich on the second atomic layer than the first layer. Still, as shown in the plot, both curves are above the dash line, which indicates that the surface Pt concentration of first and second layer are both higher than the bulk Pt concentration. We want to know if the temperature has effects on this phenomenon, so we did anther two cases for Pt_xNi_{100-x} alloys at 1000 K and 1400 K besides 1200 K. Figure 3.10 (b) and (c) visualized the segregation profile for 1000 K and 1400 K, respectively.

From the distance that the curves away from the dash lines in Figure 3.10 we can see that as the temperature increases, the surface segregation becomes weak. And the tendency of Pt atoms segregated more on the second layer begins at lower bulk Pt concentration as temperature increases.

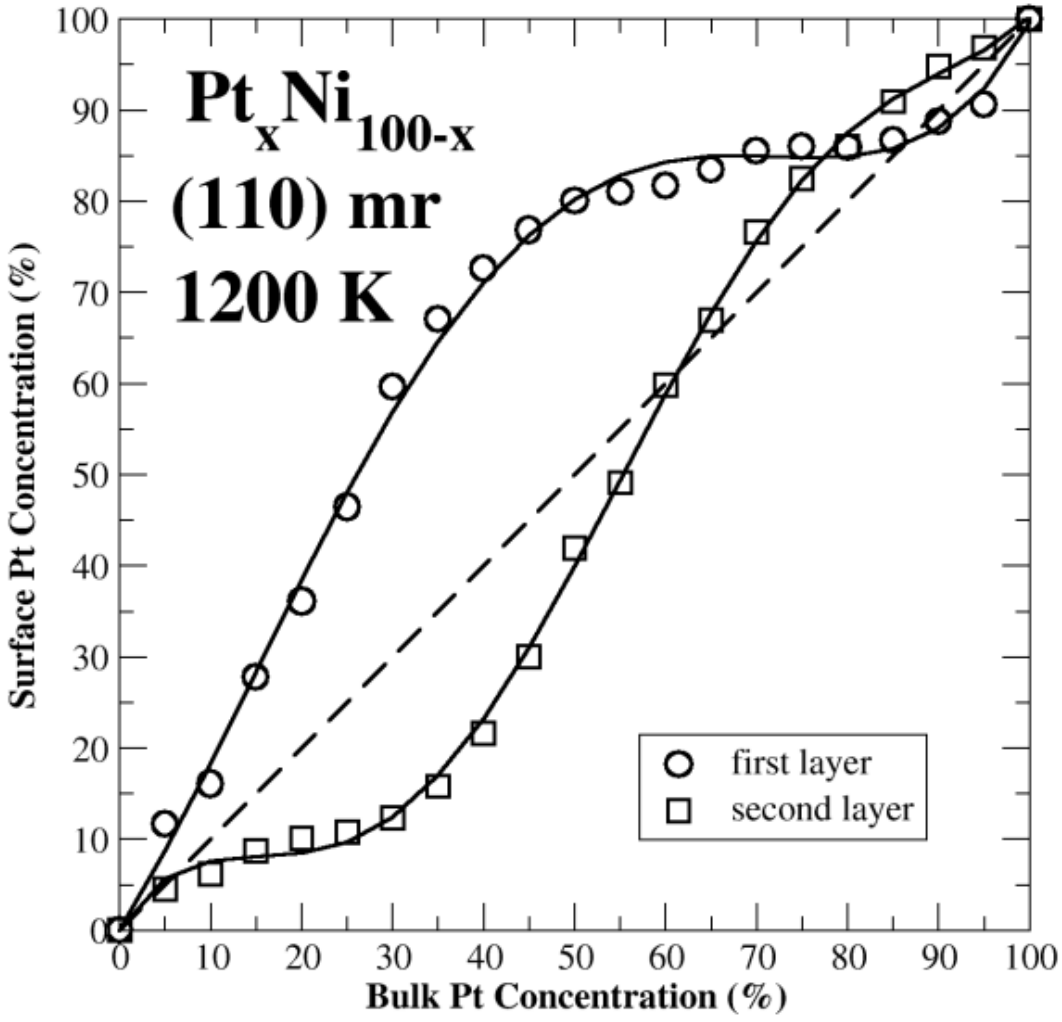

(a) T = 1200 K

Figure 3.10 (a) – (c) Surface concentrations versus bulk concentrations of Pt for Pt_xNi_{100-x} (110) (1x2) missing row surface at different temperatures

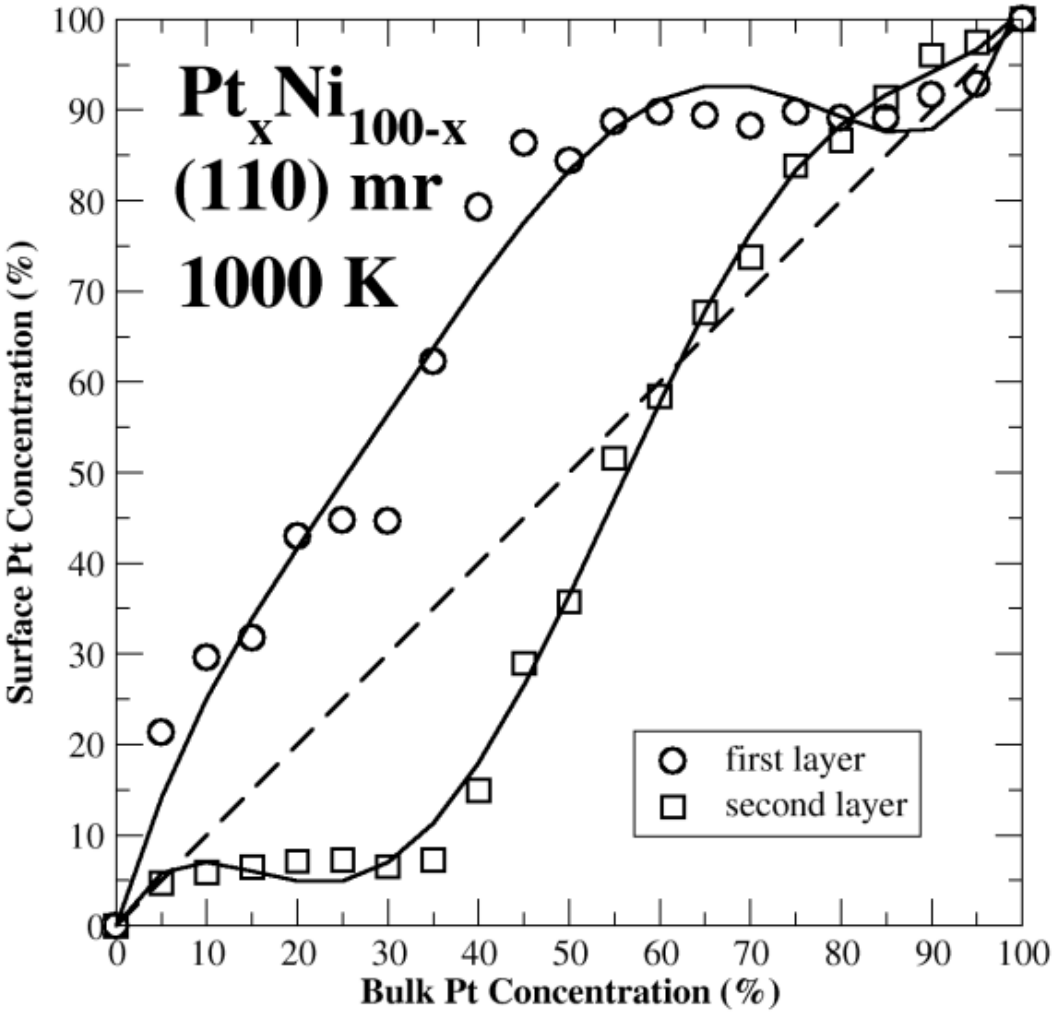

(b) T = 1000 K

Figure 3.10 (a) – (c) Continued

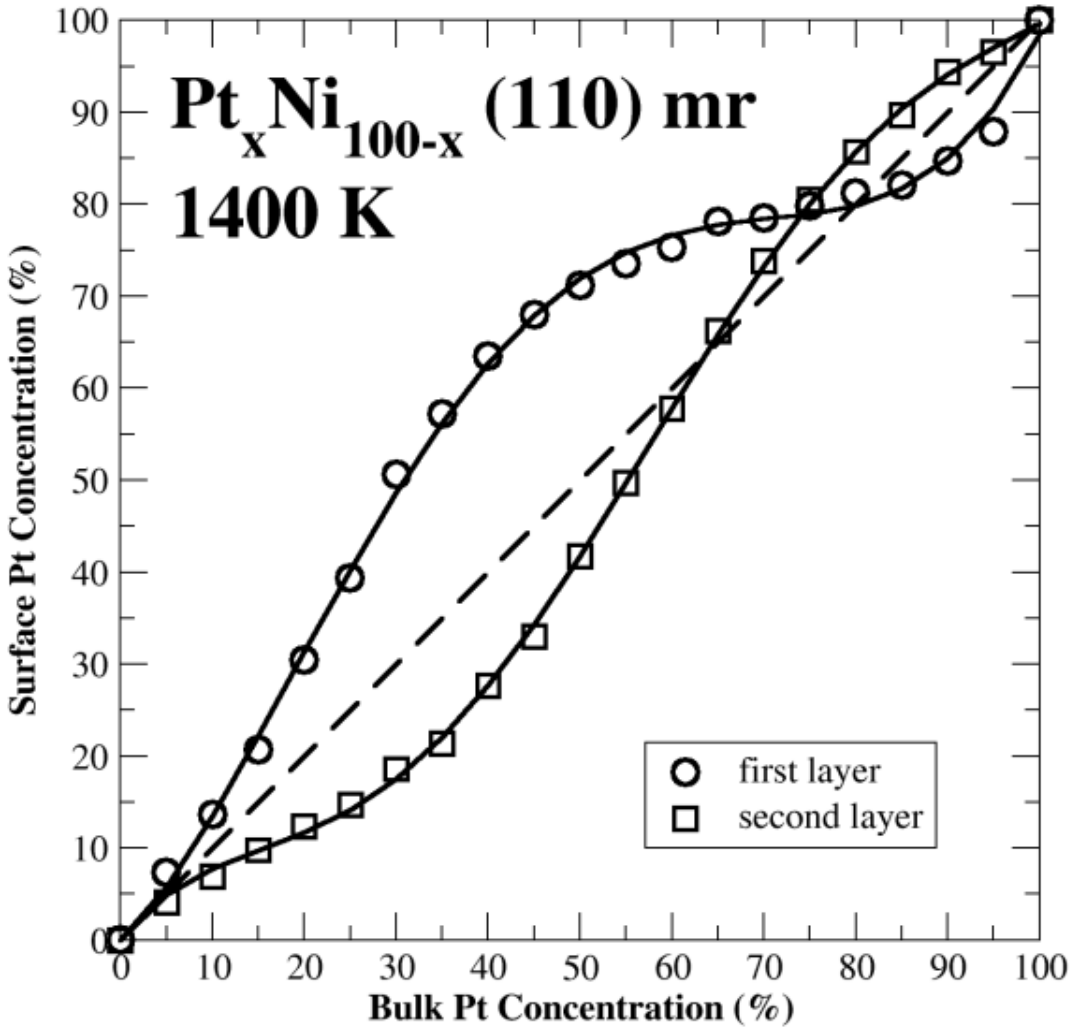

(c) T = 1400 K

Figure 3.10 (a) – (c) Continued

3.3.2.4 Interlayer Relaxations for Pt-Ni (111), Unreconstructed and Reconstructed (110) Surfaces

For the Pt_xNi_{100-x} alloys, we employed interlayer relaxation during the surface segregation MC simulation, which allows the slab to vibrate perpendicularly to the according surface. Since it is important to examine the final relaxation status, we plot the interlayer relaxation between every two layers of the first three atomic layers with respect to the bulk Pt concentration for (111), (110) and (110) (1x2) missing row surface in

Figure 3.11. The circles present the interlayer relaxation between the first two layers, while the diamonds present the interlayer relaxation between the second and the third layer. The solid lines are polynomial function fitting to these data points.

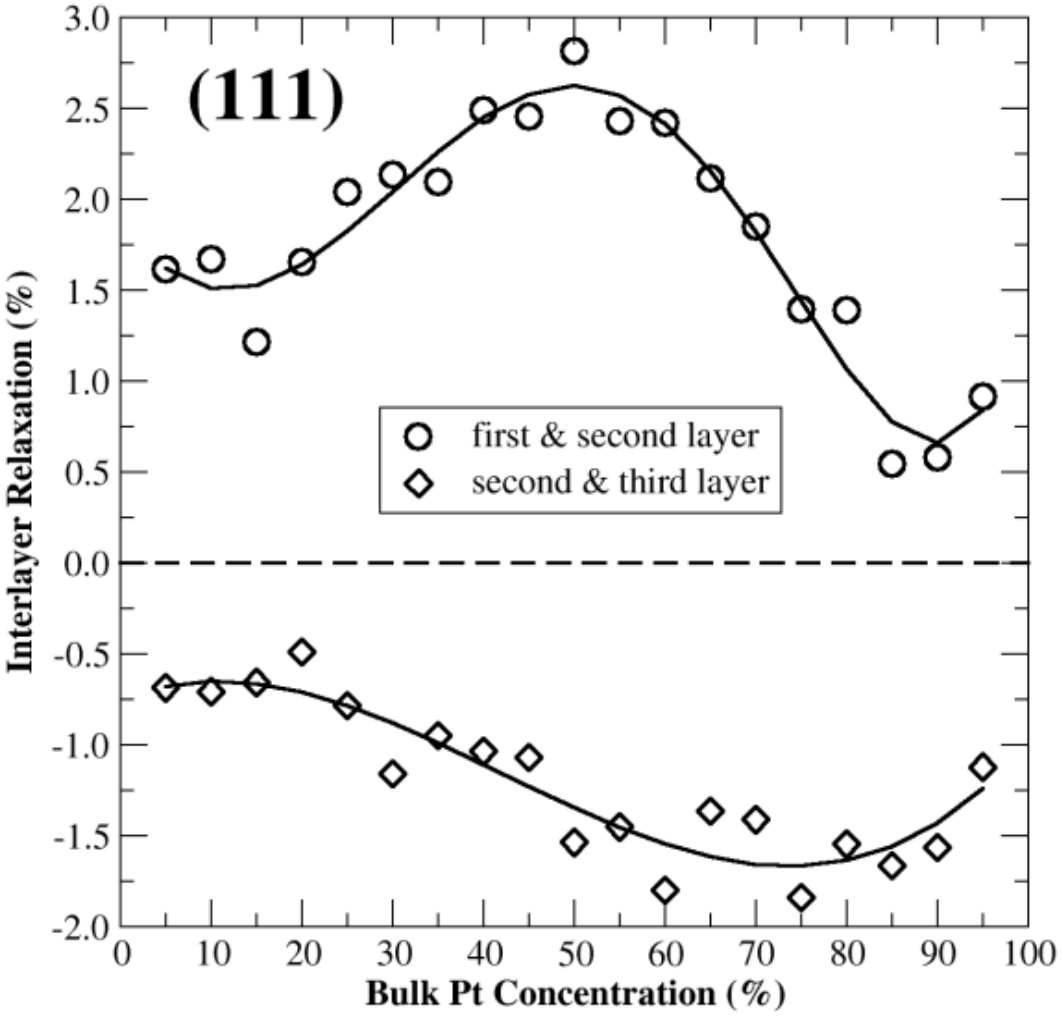

(a) (111) surface

Figure 3.11(a) – (c) Interlayer relaxations versus bulk Pt concentrations on different surfaces at 1200 K

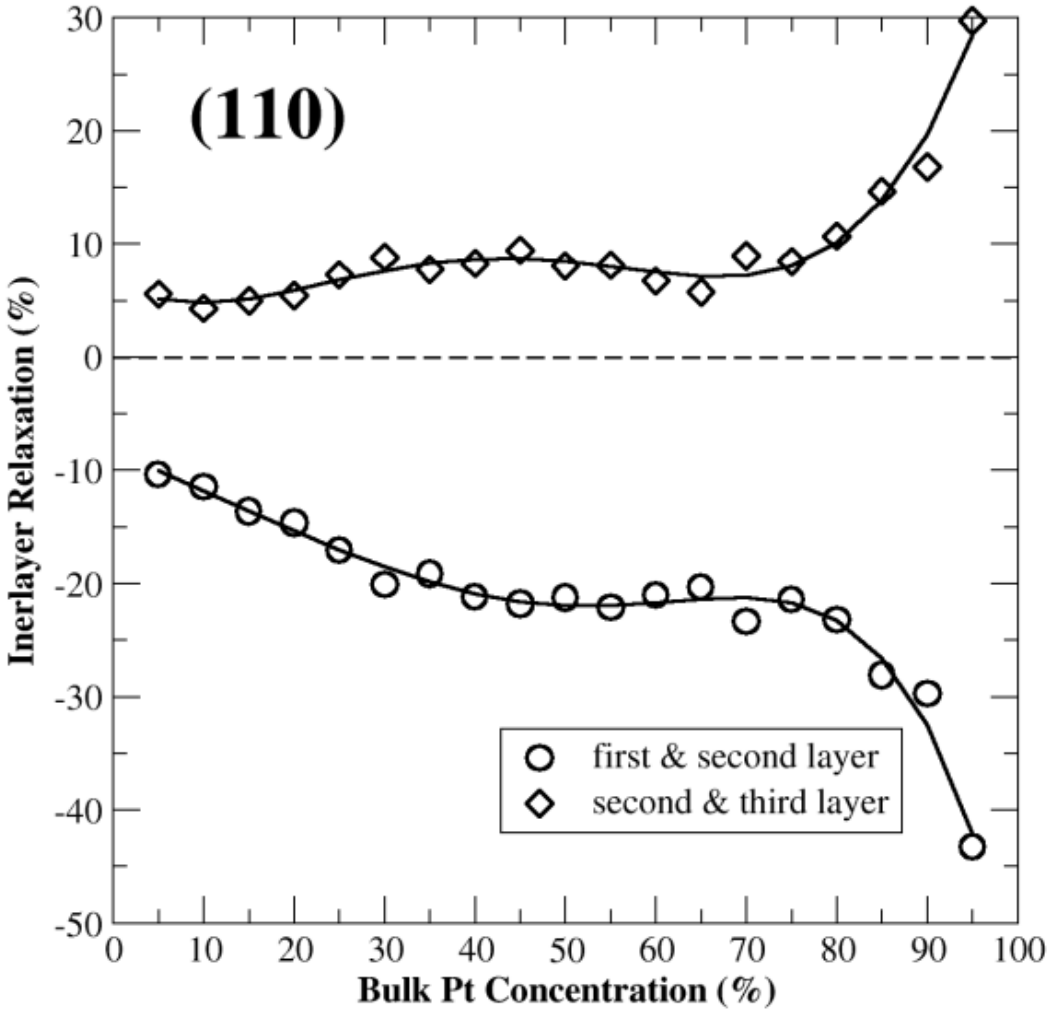

(b) (110) surface

Figure 3.11 (a) – (c) Continued

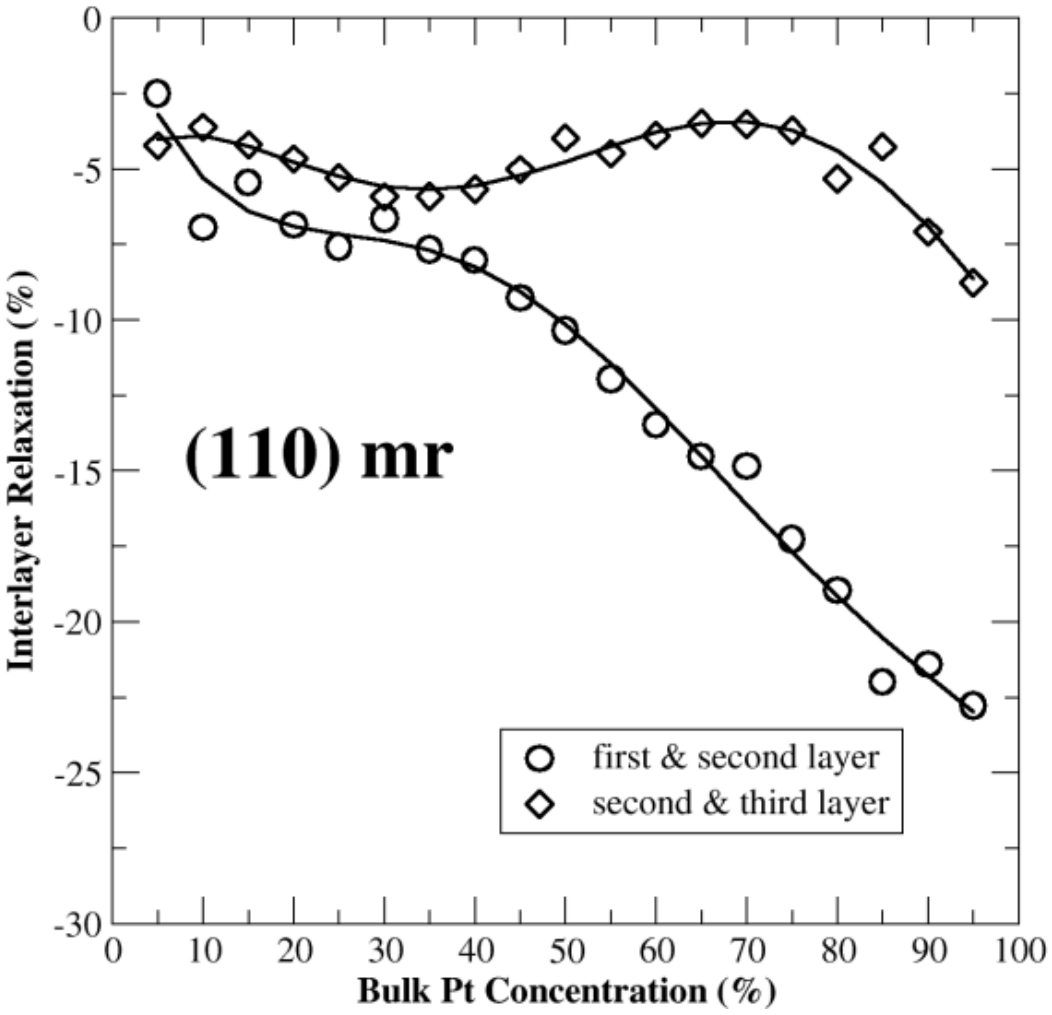

(c) (110) missing row surface

Figure 3.11 (a) – (c) Continued

As can be seen in Figure 3.11 (a), on the Pt_xNi_{100-x} (111) surface, the interlayer distance between the outmost and second layer are extended, and as the increase of bulk Pt concentration, the relaxations exhibit a wavelike tendency with the highest extension at the composition of 50%. The outwards relaxation may be caused by the size effect of Pt. Since the Pt atoms which have larger size than Ni atoms segregate to the outmost layer, the space between the first two layers tends to extend to lower the strain energy. The space between the second and third layer is contracted, and the higher is the bulk Pt

concentration, the less space between these two layers. The strongest contraction occurs between 70 at.% to 75 at.% concentration of bulk Pt.

With two solid lines separated by the dash line in Figure 3.11 (b) also, but exhibits reverse relaxation tendency at (110) surface compared to that of (111) surface. Along with the Pt atoms segregate to the subsurface, the interlayer distance between the second and third layer is enlarged, while the space between the first two layers is decreased. As mentioned above, the size difference of Pt and Ni atoms is the dominant factor driving this phenomenon.

However, for reconstructed (110) (1x2) surface, both interlayer distances are contracted (see Figure 3.11 (c)), which should be similar to the (111) surface, if explained by the size effect. Moreover, the interlayer distance between the first and second layer exhibit a stronger contraction than the that of subsurface interlayer spacing, which is in agreement with the claim made by Baudoing et al. [11]. Though more Pt atoms segregate to the outmost layer, for the more opened reconstructed (110) surface, the coordinate number of the atoms on the second layer is not large enough, the Pt atoms at the surface tend to move close to the atoms (mainly Ni atoms) at the second layer to increase the coordinate number and maximize the number of Pt-Ni bond at the same time.

4. ADSORPTION ENERGY

4.1 Methodology

Density functional theory was the method we applied in this work to determine the electron density of the system. As described in Equation 4.1, the electron density of a system can be obtained by solving a series of Schrodinger equations, as shown in Equation 4.1 [41].

$$\left\{-\frac{1}{2}\nabla^2 + v_{ext}(r) + v_H(r) + v_{xc}(r)\right\}\psi_i(r) = \varepsilon_i\psi_i(r) \qquad \text{Eq. 4.1}$$

Here, the external potential $v_{ext}(r)$ is

$$v_{ext}(r) = -\sum_a \frac{Z_a}{|r - R_a|} \qquad \text{Eq. 4.2}$$

Hartree potential

$$v_H(r) = \int \frac{\rho(r')}{|r - r'|} d^3r' \qquad \text{Eq. 4.3}$$

and $v_{xc}(r)$ is the exchange-correlation potential

There is no approach to exactly derive the exchange-correlation potential at present, so in practice, several types of functionals were introduced to approximate it, such as Generalized Gradient Approximation (GGA), Local Density Approximation (LDA). All the terms in the equations above, no matter how large the system is, are only dependent on the three-dimensional coordinates, which can largely reduce the computer cost.

Based on the Hohenberg-Kohn theorems, the key points in DFT were: 1) the electron density that produce the minimum energy of the system is the correct one; 2) as

long as we obtain the correct density, the ground state and other electronic properties of the system can be determined.

4.2 Computational Models

The *Vienna ab Initio Simulation Package* (VASP) software, one of the most efficient codes to perform DFT calculations is used in this work. To carry out all adsorption energy calculations, using VASP, the optimized electron structures were obtained according to the spin polarized DFT at the generalized gradient approximation (GGA) level. Ultrasoft pseudopotentials and projector augmented wave (PAW) method were employed to describe the exchange and correlation functional. An energy cutoff of 400 eV was used in all calculations in order to get accurate values for adsorption energies while keeping the computer cost as low as possible. Structure optimization was terminated when the force acting on each atom becomes less than 0.01 eV/Å. We used a 16 x 16 x 16 k-point mesh for equilibrium lattice constant calculation of platinum and 5 x5 x 1 k-point mesh for adsorption energy calculations.

The (111) and (100) surfaces of Pt and Pt-based alloys were modeled using a periodic slab with a 2 x 2 surface unit cell in fcc lattice and four layers with four metal atoms on each layer. The initial separations of atoms in the slab are determined by the calculated equilibrium lattice constants of Pt. In our supercell surface model, shown in Figure 5.1, there was a vacuum region with a thickness of 12 Å. In order to model surface adsorption, we placed the adsorbed atom or molecule on the top of one side of the surface slab. Thus, we simulated a 0.25 monolayer coverage of surface adsorption on the catalyst surfaces. During the structural optimization, the adsorbates and the two uppermost layers were allowed to fully relax, while the two lowest atomic layers were kept fixed at their positions determined from equilibrium crystal lattice during structure optimization. For the Pt-based alloys (Pt-Co, Pt-Ni, and Pt-Fe), surface segregation phenomenon were introduced for both surfaces with the second layer containing only the alloyed metals (shown in Figure 4.1 highlighted by red color) and pure Pt skin on the outmost layer. The

adsorption energy of the adsorbed species can be calculated as the difference between the energy difference of the adsorbed system (surface with adsorbed species) and the sum of the free surface and the energy of the gas-phase species, as shown in Equation 4.1.

$$E_{ads} = E_{adsorbate\text{-}surface} - E_{surface} - E_{gas\text{-}phase\ molecure} \quad \text{Eq. 4.1}$$

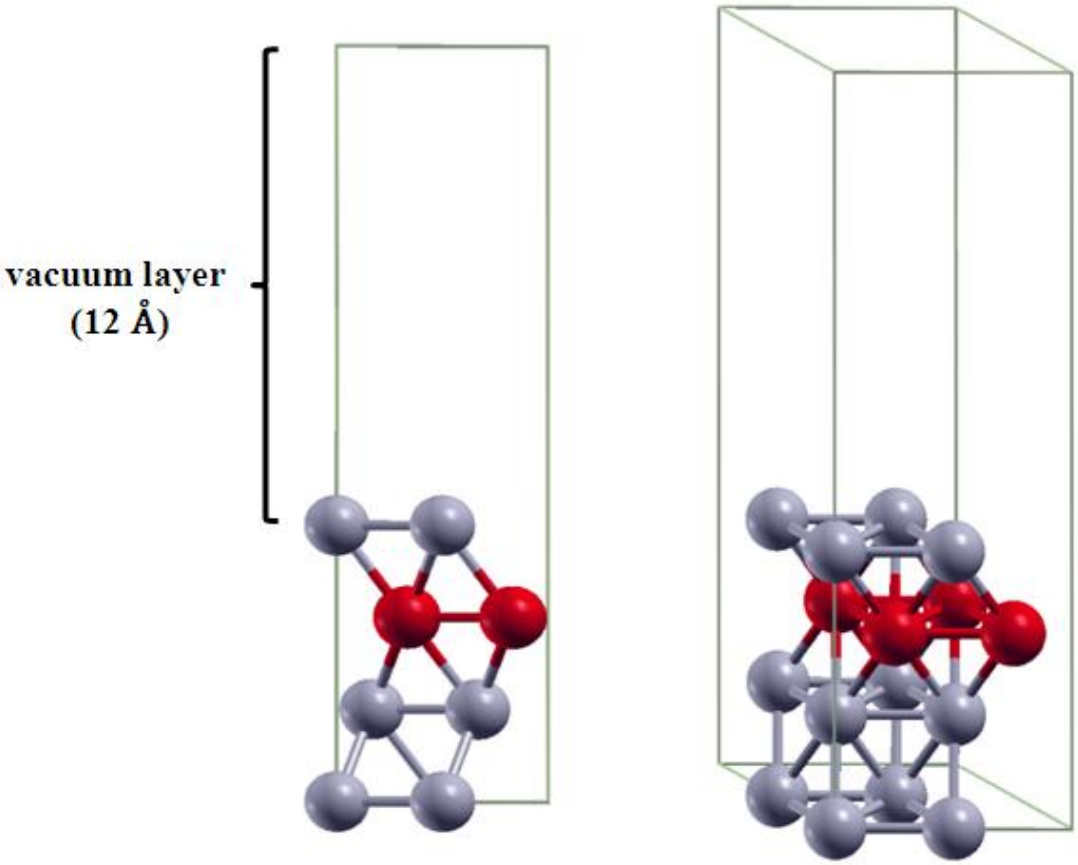

(a) (111) surface

Figure 4.1 (a) and (b) The unit cell containing four atomic layers
for (111) and (100) surfaces

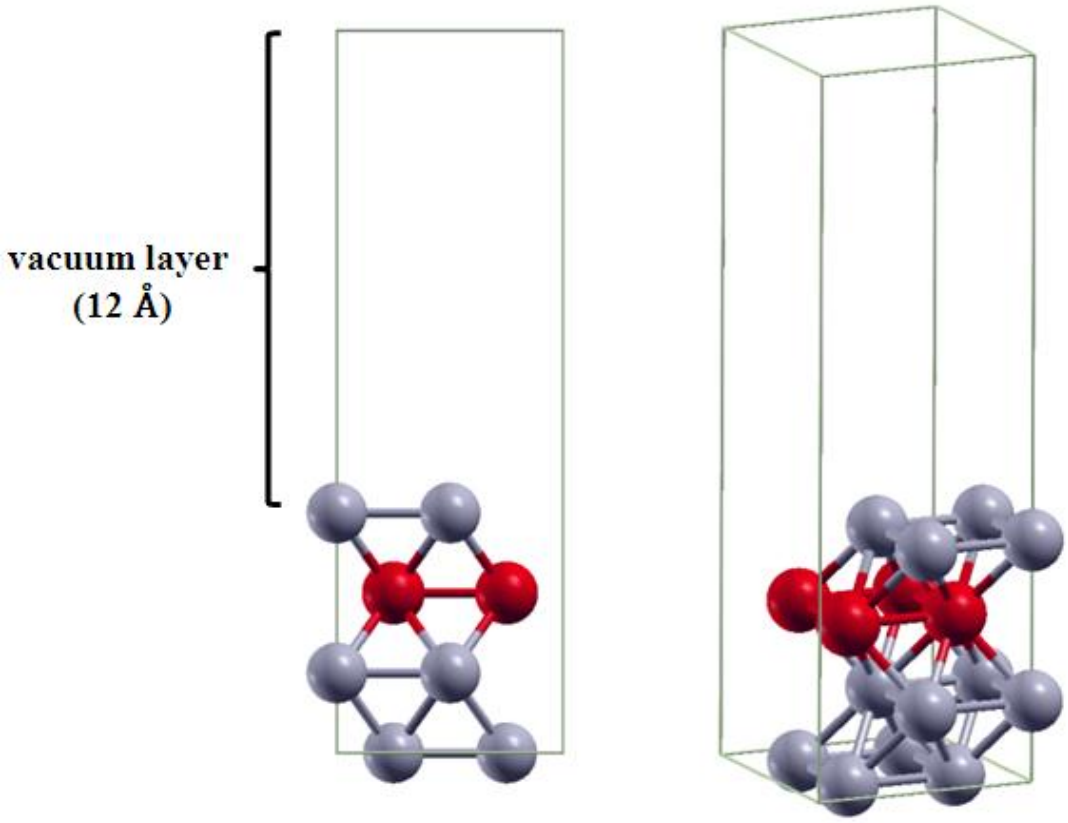

(b) (100) surface

Figure 4.1 (a) and (b) Continued

4.3 Results and Discussion

4.3.1 Equilibrium Lattice Constant of Pt

Figure 4.2 shows the result of equilibrium lattice constant searching for fcc platinum. As we can see, the free energy of the system converged to a minimum value at a lattice constant of 3.992 Å. Compared to experimental lattice constant of 3.92 Å, the quantum mechanics value is within a reasonable 1.84% error.

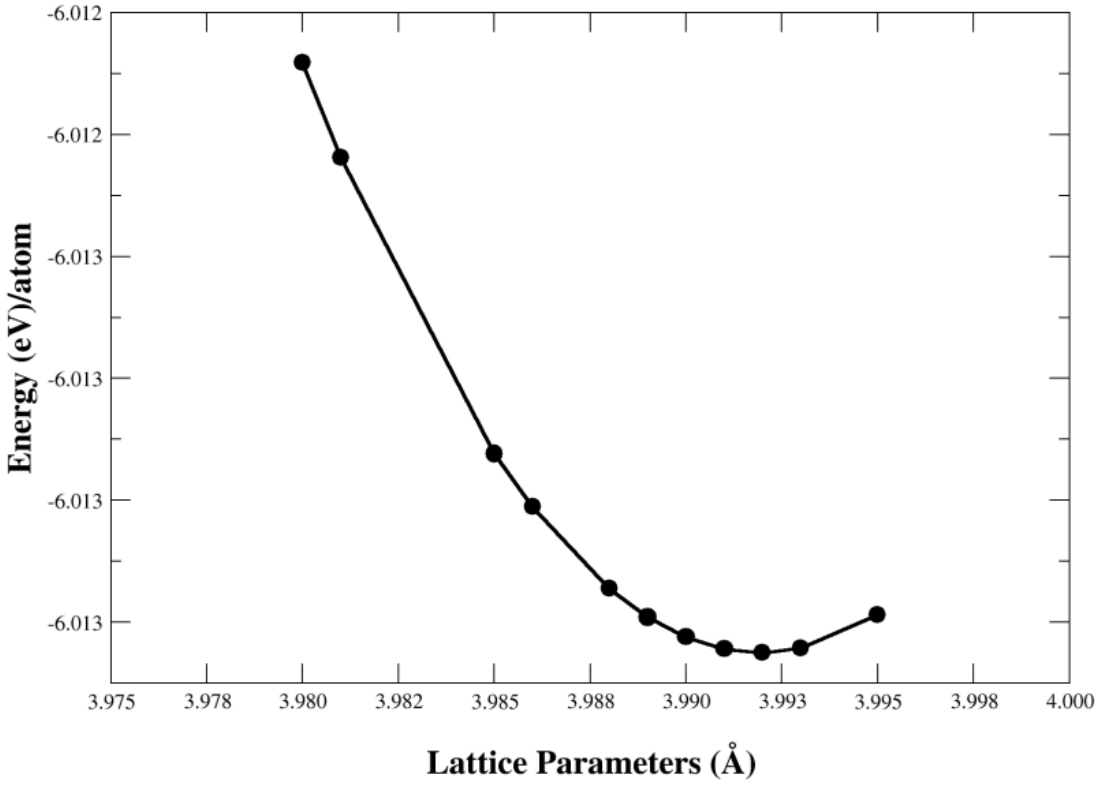

Figure 4.2 Energy convergence for lattice parameter calculations for Pt

4.3.2 Adsorption Site

In this work, we studies the adsorption of four species (O, O_2, OH, H_2O) on the (111) and (100) surfaces of Pt and Pt-based alloys (Pt-Co, Pt-Ni and Pt-Fe). Among the four species, O, OH and H_2O will be adsorbed on the surface with single oxygen atom binding to the surface, while O_2 molecule will be adsorbed by the whole molecule binding.

On the (111) surface, we have four distinct low-energy adsorption sites for the single oxygen atom binding. Shown in Figure 4.3 (a), the four different adsorption sites are denoted as fcc, hcp, bridge and top [42]. The fcc site is a three-fold symmetry site where the species are adsorbed without one metal atom beneath in the subsurface layer. The hcp site is also a three-fold symmetry site, but there is one atom beneath the species

in the subsurface layer. The bridge site is a two two-fold symmetry site with species adsorbed lying in the middle between two adjacent surface atoms. The top site is a single symmetry site where the species are adsorbed right above one surface atom. For convenience, we use f, h, b and t in the following paragraph to indicate fcc, hcp, bridge and top site, respectively. For oxygen molecule adsorption, there are three typical low-energy adsorption sites [43]: tfb, thb and tbt. See Figure 4.3 (b), oxygen molecules are represented with green balls and sticks. The tfb site indicates that one oxygen atom lies on top of one surface atom while the other oxygen atom lies near the bridge site. The O-O bond lies above an fcc adsorption site (where there is no atom on the subsurface). The thb site is where one atom lies above one surface atom while the other oxygen atom lies near the bridge site. The difference from tfb is that the O-O bond lies above an hcp adsorption site (where there is one atom on the subsurface layer). For the tbt adsorption site, two oxygen atoms lie above the tops of two adjacent surface atoms and the O-O bond is aligned along the connecting line between those two surface atoms.

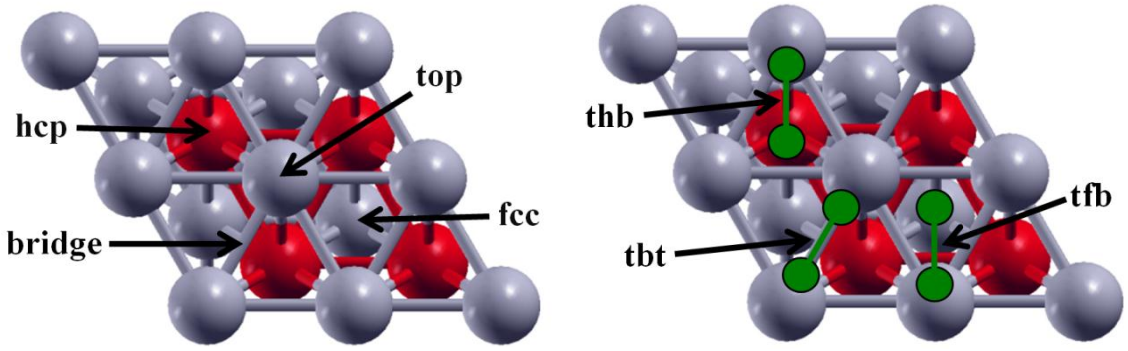

(a) for O, OH and H_2O (b) for O_2 molecule

Figure 4.3 (a) and (b) Adsorption sites on (111) surface

For (100) surface, we have three adsorption sites for single oxygen atom bonding: top, hollow and bridge. The top site is just in top of a surface atom; on the center of four adjacent surface atoms where there is an atom at the subsurface is called hollow ("hollow"

means there is no atom on the surface layer); bridge site is where the adsorbed species lie in the middle between two adjacent surface atoms, as shown in Figure 4.4 (a).

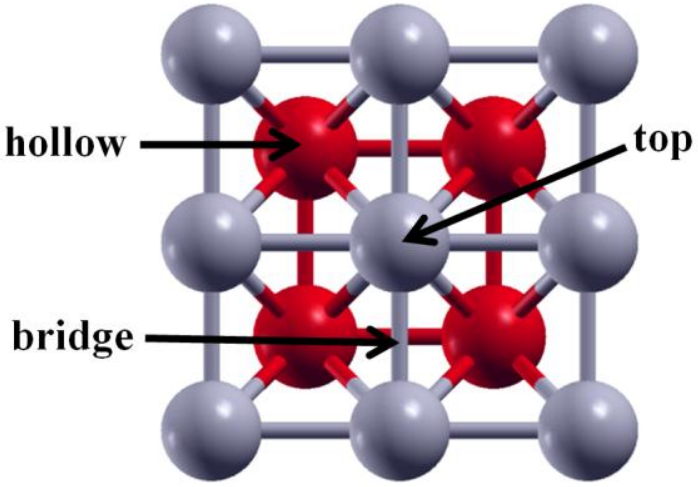

(a) for O, OH and H_2O

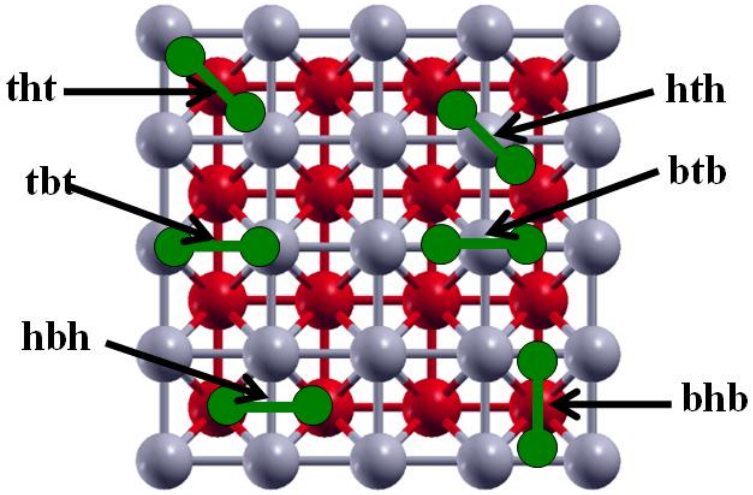

(b) for O_2 molecure

Figure 4.4 (a) and (b) Adsorption sites on (100) surface

Figure 4.4 (b) gives the adsorption site for O_2 molecure on (100) surface. In order to show the sites clearly, we use the top view of the surface generated by 4 x 4 unit cell. There are six possible sites that might produce low adsorption energy. Here t, h, and b indicate top, hollow, and bridge, respectively.

1) tht: two oxygen atoms lie above the metal atoms on the surface with their bond above the hollow site
2) tbt: two oxygen atoms lie above the metal atoms on the surface with their bond aligned along the connecting line between those two surface atoms
3) hbh: two oxygen atoms lie above the hollow sites with their bond aligned along the connecting line between the adjacent metal atoms on the subsurface (here "b" means the O-O bond cross the bridge site on the surface)
4) hth: two oxygen atoms lie above the hollow sites with their bond cross the metal atom on the surface
5) btb: two oxygen atoms lie above the bridge sites while the O-O bond crosses a metal atom on the surface
6) bhb: two oxygen atoms lie above the middle point of two bridge sites with the O-O bond above the hollow site.

4.3.3 Adsorption Energy for (111) Surface of Pure Pt

4.3.3.1 Adsorption Energy of Atomic Oxygen

We first carried DFT calculation of oxygen adsorption on top, bridge, fcc, and hcp sites on the surface of pure Pt to determine the most stable configuration. Table 4.1 lists the energy and bond length of Pt-O for each adsorption site. For comparison, values obtained by others listed in the brackets.

Table 4.1 Calculated adsorption energy E_{ad} of atomic oxygen on Pt(111) surface using first principles DFT method.

Adsorption Site	top	bridge	fcc	hcp
E_{ad} (eV)	-2.643	unstable	-3.967 (-3.88 [27])	-3.556 (-3.48 [27])
D_{Pt-O} (Å)	1.84		2.05	2.06

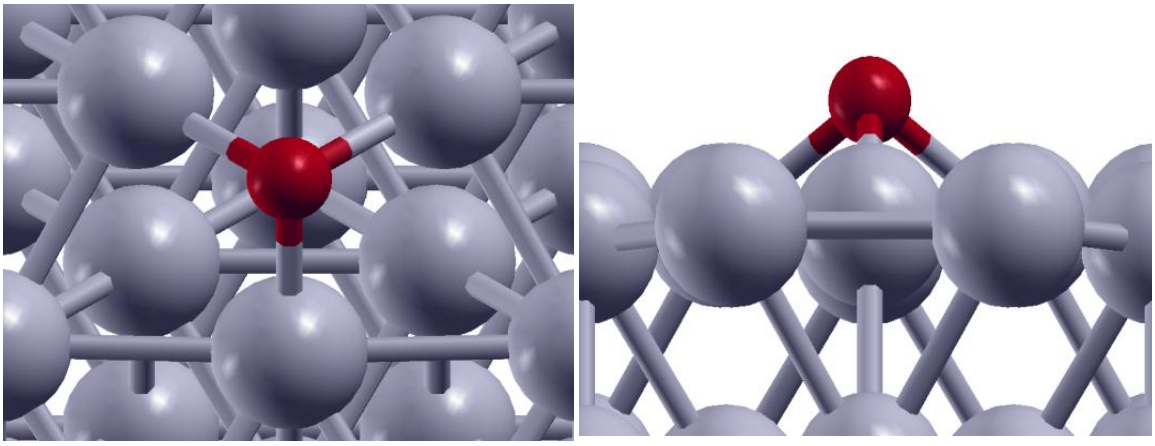

(a) top view (b) side view

Figure 4.5 (a) and (b) Configuration of atomic oxygen adsorption at the fcc site on Pt(111) surface

The adsorption of single oxygen atom on the surface of transition metals has been widely studied before [26 - 27, 43]. Consistent with those work, we found that the most energetically favorable site for oxygen atom adsorption on the Pt(111) surface is the fcc site, with the adsorption energy of -3.967 eV; following behind is the hcp adsorption site, which has an increase of 0.411 eV. The adsorption energy of oxygen atom at the top surface site is -2.643 eV, which is even higher than hcp site. Moreover, the adsorption at the bridge site is very unstable, and it finally relaxed to fcc site in our calculation. In Table 4.1, we also give the bond length of Pt-O. The fcc and hcp configurations have larger bong length than that of the top configuration due to their special geometry. Figure 4.5 shows the optimized geometry of fcc adsorption on the Pt(111) surface for oxygen atom.

4.3.3.2 Adsorption Energy of Hydroxyl Molecule

The situation for hydroxyl molecule is more complicated than that of oxygen atom, because we have to consider the rotation of the O-H bond, which may affect the adsorption energy. Table 4.2 lists the calculated adsorption energy for different

configurations. The results of similar work done by Michaelides [29] are given in the brackets for comparison. The most stable geometries for fcc and hcp sites are oxygen atom adsorbed in the corresponding sites, both with the O-H bond perpendicular to the Pt(111) surface, the high symmetry of which leads to the lowest energy. The most favorable geometry for the adsorption of OH molecule is found to be the bridge and top sites with adsorption energies of -2.384 and -2.400 eV. We cannot determine which site is more energetically favorable since there is only a difference of 0.006 eV. Figure 4.6 and Figure 4.7 are the top and side views of geometries for OH adsorption at top and bridge sites after final optimization, respectively.

Table 4.2 Calculated adsorption energy E_{ad} of hydroxyl on Pt(111) surface using first principles DFT method

Adsorption Site	top	bridge	fcc	hcp
E_{ad} (eV)	-2.384 (-2.27)	-2.400 (-2.22)	-2.088 (-2.00)	-1.843 (-1.80)
D_{Pt-O} (Å)	2.00	2.18	2.23	2.31
D_{O-H} (Å)	0.97	0.98	0.97	0.97

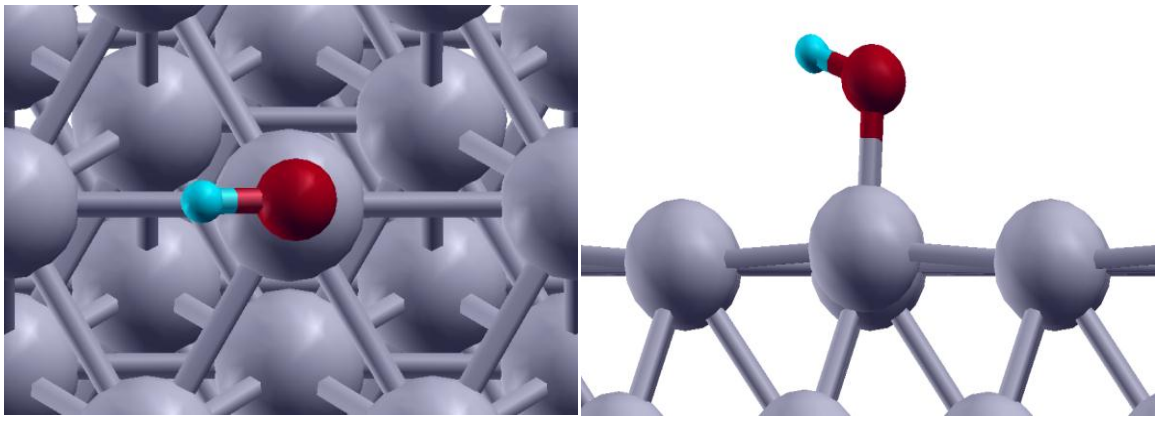

(a) top view (b) side view

Figure 4.6 (a) and (b) Configuration of OH adsorption at the top site on Pt(111) surface

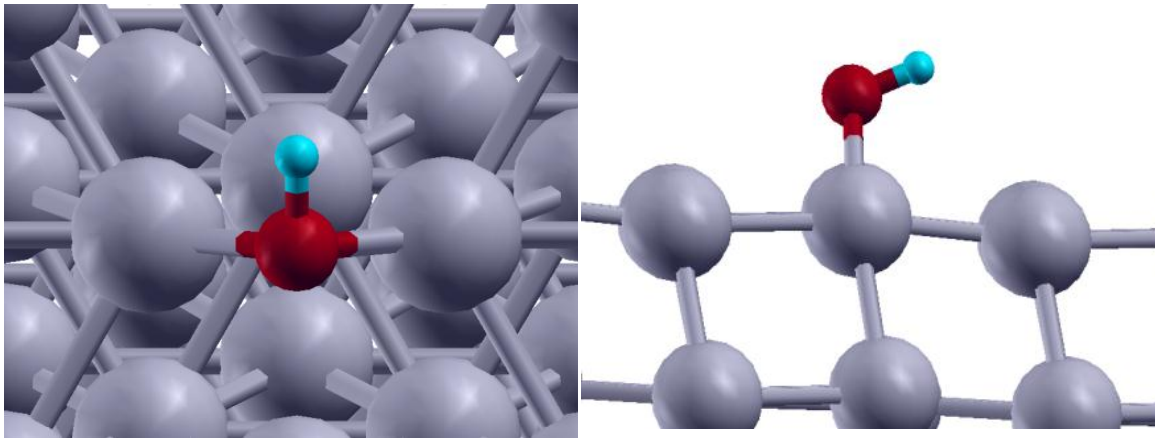

(a) top view (b) side view

Figure 4.7 (a) and (b) Configuration of OH adsorption at the bridge site on Pt(111) surface

As we mentioned before, we tried different rotation angles for O-H bond, the results turned out that: for the top site, the most stable structure is the O-H bond aligning along the Pt-Pt bond with an angle of 106^{o} away from the (111) surface, see Figure 4.6; for the bridge site, the energetically favorable geometry is the O-H bond pointing to the hcp site, with an angle of 105^{o} between H, O and the Pt atom that has been adsorbed to, shown in Figure 4.7.

4.3.3.3 Adsorption Energy of Water Molecule

Water molecule is the product of ORR process. When H_2O is absorbed onto the Pt(111) surface, it is most likely to be at a top site with O end down and the molecule plane almost parallel to the surface. Shown in Figure 4.8, the H_2O molecule plane tilts by 5^{o} away from the surface plane and H-O-H bond angle of water molecule is determined to be 104.98^{o} in this work. Generally speaking, the interaction between water molecule and Pt surface is very weak: the adsorption energy is -0.287 eV.

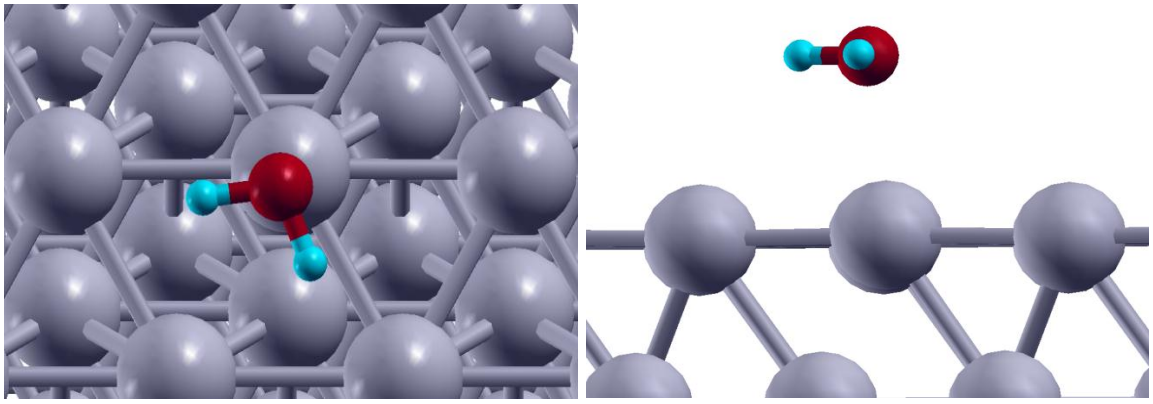

(a) top view (b) side view

Figure 4.8 (a) and (b) Configuration of H_2O adsorption at the top site on Pt (111) surface

4.3.3.4 Adsorption Energy of Oxygen Molecule

The adsorption of O_2 on the catalyst surface is claimed as the first step of ORR process. For oxygen molecule, the adsorption energies given by our DFT calculations are -0.655 eV at tbt site, -0.660 eV at tfb site, and -0.506 eV at thb site.

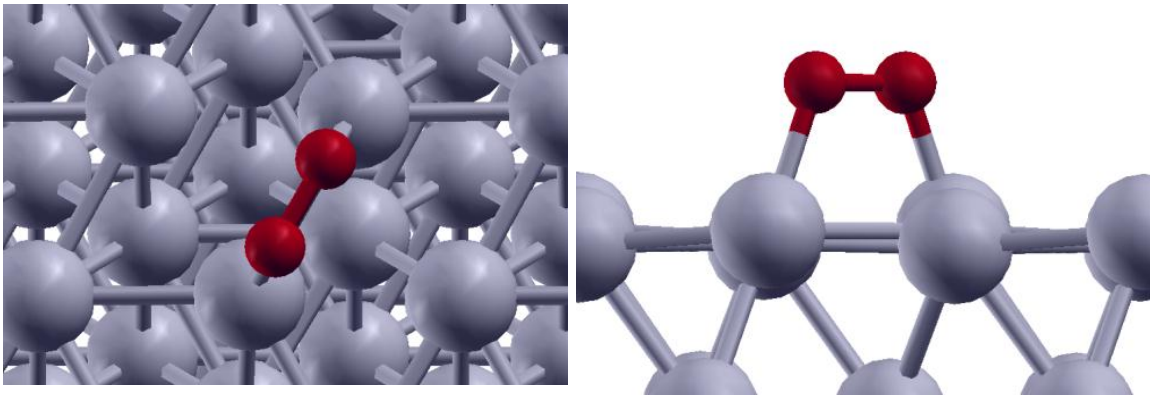

(a) top view (b) side view

Figure 4.9 (a) and (b) Configuration of O_2 adsorption at the tbt site on Pt (111) surface

Table 4.3 Calculated adsorption energy E_{ad} of oxygen molecule on Pt(111) surface using first principles DFT method.

Adsorption Site		tbt	tfb	thb
E_{ad} (eV)		-0.655	-0.660	-0.506
Bond Length	O_1-O_2	1.35	1.39	1.38
(Å)	O_1-Pt	2.06	2.03	2.06
	O_2-Pt	2.06	2.19	2.24
Tilting Angle (^{o})		0.0	10.3	9.3

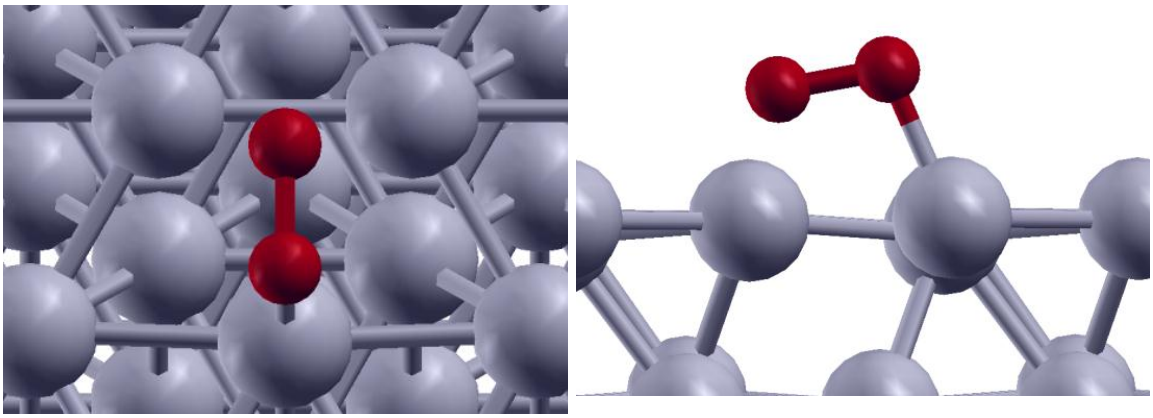

(a) top view (b) side view

Figure 4.10 (a) and (b) Configuration of O_2 adsorption at the tfb site on Pt (111) surface

4.3.3.5 Summary

For the (111) surface of pure Pt, the adsorption energy of four species in ORR process have been investigated based on the framework of first principles. The most stable configurations for O and H_2O are the top site. When adsorbed with OH, the bridge is the most energetically favorable site, closely followed with an increase of 0.006 eV is the top site. For O_2 molecule, the tfb and tbt sites have lower adsorption energies than the thb site.

4.3.4 Adsorption Energy for (111) Surfaces of Pt-M Catalysts

Since we have already studied the adsorption system for the pure Pt, we will further investigate the (111) surface of Pt-base alloys (Pt-Ni, Pt-Co and Pt-Fe) based on some conclusions we made in Section 4.3.3.5. In this work, only the sites with low adsorption energies will be examined: top site for O atom and H_2O molecule; top and bridge sites for OH; tbt and tfb sites for O_2 molecule.

Table 4.4 Adsorption energies (eV) of ORR species on (111) surface for pure Pt and Pt-Ni, Pt-Co and Pt-Fe alloys

Catalyst	O	OH		H_2O	O_2	
	fcc	bridge	top	top	tbt	tfb
Pt	-3.967	-2.400	-2.384	-0.287	-0.655	-0.660
Pt-Ni	-3.502	-2.142	-2.153	-0.237	-0.277	Unstable
Pt-Co	-3.378	-2.219	-2.217	-0.261	-0.274	Unstable
Pt-Fe	-3.191	-2.099	-2.098	-0.225	-0.186	Unstable

Table 4.4 shows the calculated adsorption energies for O atom, OH, H_2O and O_2 molecule on the (111) surface of Pt-Ni, Pt-Co and Pt-Fe catalysts. For comparison, the results of previously studied Pt(111) surface are also included here. As can been seen in the table, the adsorption energies of each species for the Pt-based alloys are lower than that of pure Pt. First, we will focus on the adsorption of oxygen molecule. We want the ORR process to take the "direct 4-electron pathway" (dissociation mechanism) because it has the highest potential among all the pathways. In other words, instead of the adsorption of the whole oxygen molecule on the catalyst surface, we prefer the splitting of O-O bond. From Table 4.4, we can see that the O_2 adsorption on the (111) surface of Pt-Ni, Pt-Co and Pt-Fe alloys are much weaker that of pure Pt. It is likely that the ORR process may follow the dissociation mechanism on the surface of those three Pt-based alloys while the ORR process may begin with adsorption of oxygen molecule on the surface of pure Pt, which accounts for the higher ORR activity of the Pt-based alloys. The

adsorption of OH is another important issue in ORR. Both dissociation and association mechanisms involve the hydrogenation of adsorbed OH to H_2O. From the above adsorption energy results, it can be seen that OH binds more strongly on Pt(111) compared to the (111) surface of Pt-Ni, Pt-Co and Pt-Fe, which indicates more energy needed to complete the hydrogenation of OH on Pt(111) than that of Pt-based alloys. Though for Pt, Pt-Co and Pt-Fe, the adsorption energy of OH at the bridge site is lower than the top site, we consider the adsorption of OH occurs at the top site. Because the oxygen is most stable at the top site, instead of moving to bridge site to form OH ($O^* + H^+ + e \rightarrow OH^*$), it is more possible that the oxygen atom stays at the original position.

4.3.5 Adsorption Energy for (100) Surfaces of Pure Pt

4.3.5.1 Adsorption Energy of Atomic Oxygen

Table 4.5 Calculated adsorption energy E_{ad} of atomic oxygen on Pt(100) surface using first principles DFT method

Adsorption Site	top	bridge	hollow
E_{ad} (eV)	-2.906 (2.860)	-3.919 (3.809)	-3.499 (3 .155)
D_{Pt-O} (Å)	1.83	1.96	2.24

Table 4.5 shows the adsorption energies and geometry parameters for O atom at top, bridge and hollow sites. The values in brackets were calculated by Ge et al. [44] for comparison. It is clear that O atom binds most strongly to the (100) surface at bridge site with an adsorption energy of -3.919 eV, while the top site is the least energetically favorable adsorption site. The optimized structure of the adsorption system at the two-fold bridge site is shown in Figure 4.11. The bond length of Pt-O is 1.96 Å.

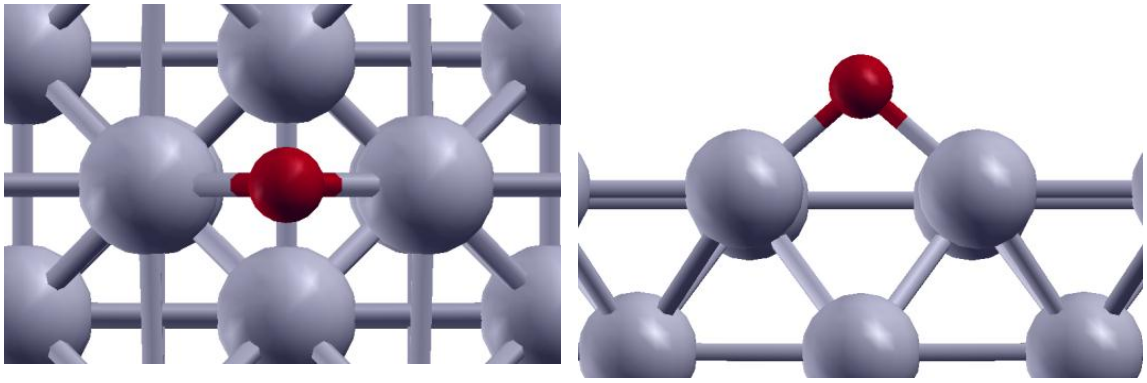

(a) top view (b) side view

Figure 4.11 (a) and (b) Configuration of atomic oxygen adsorption at the bridge site on Pt (100) surface

4.3.5.2 Adsorption Energy of Hydroxyl Molecule

Similar as we studied OH adsorption on Pt(111) surface, different rotation directions of O-H axis have been tried in our DFT calculations. For each case (top, bridge and hollow), we put the oxygen atom at the corresponding adsorption site, while the hydrogen atom has three low-energy geometries: one is right above the oxygen atom such that the O-H axis perpendicular to the (100) surface; second is near the hollow site with an tilting angle between O-H bond and (100) surface; the last one is near another Pt atom on the surface such that the O-H bond aligned with the Pt-Pt bond. It turned out the lowest-energy adsorption occurs at bridge site and the corresponding adsorption energy is -2.935 eV. The adsorption energy will increase by 0.435 eV and 0.739 eV if OH molecule adsorbed at top and hollow site, respectively. Figure 4.12 shows the final configurations optimized by our calculation at the bridge site. The tilting angle between O-H axis and (100) surface is 21.2^{o}, and the bond length of Pt-O and O-H are 2.11 Å and 0.98 Å, respectively, as given in Table 4.6.

Table 4.6 Calculated adsorption energy E_{ad} of hydroxyl on Pt(100) surface using first principles DFT method

Adsorption Site	top	bridge	hollow
E_{ad} (eV)	-2.505	-2.935	-2.196
D_{Pt-O} (Å)	1.98	2.11	2.42
D_{O-H} (Å)	0.97	0.98	0.98

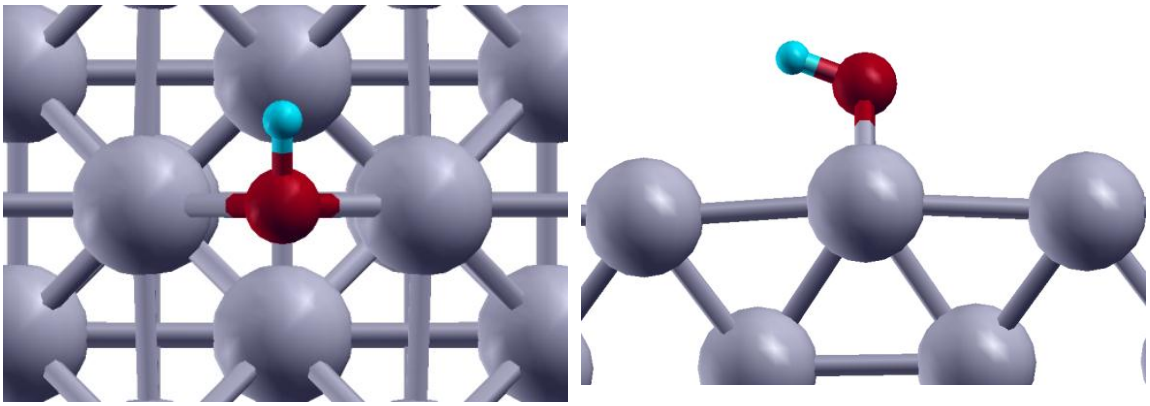

(a) top view (b) side view

Figure 4.12 (a) and (b) Configuration of OH adsorption at the bridge site on Pt (100) surface

4.3.5.3 Adsorption Energy of Water Molecule

The results for H_2O adsorption on Pt(100) surface are summarized in Table 4.7. We found that the most stable configuration for H_2O is the top site with the lowest energy of -0.307 eV. Schematic view of the energetically favorable sites is shown in Figure 5.13. In this configuration, H atoms lie to the nearest hollow sites making the H-O-H molecule plan has a 20.5 tilting angle with respect to the Pt(100) surface. We also tested the adsorption energy on the hollow site, but it turned out the energy is much higher than the top site.

Table 4.7 Calculated adsorption energy E_{ad} of water molecule on Pt(100) surface using first principles DFT method

Adsorption Site	top	hollow
E_{ad} (eV)	-0.307	-0.103
D_{Pt-O} (Å)	2.43	3.28
D_{O-H} (Å)	0.97	0.97
Angle of H-O-H (^{o})	105.1	103.8
Tilting Angle (^{o})	20.5	-22.6

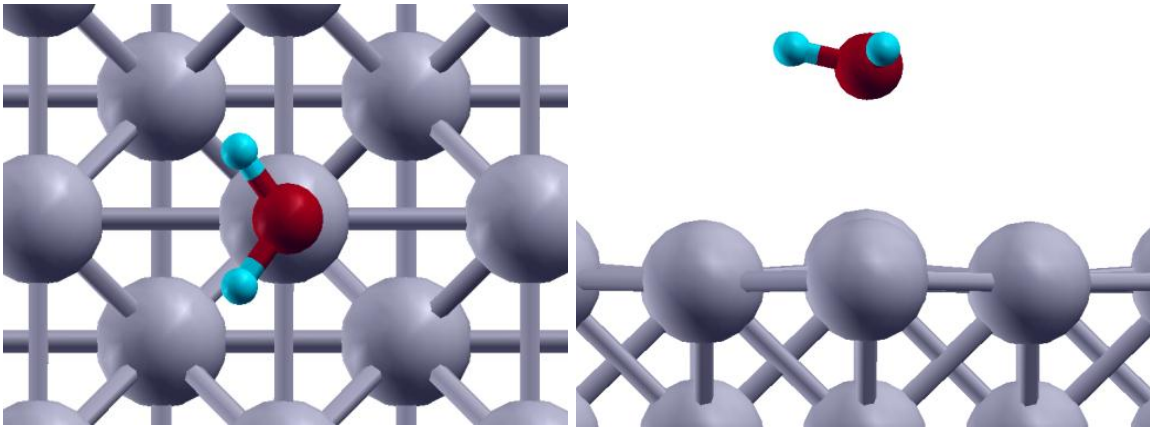

(a) top view (b) side view

Figure 4.13 (a) and (b) Configuration of H_2O adsorption at the hollow site on Pt (100) surface

4.3.5.4 Adsorption Energy of Oxygen Molecule

Six high-symmetry adsorption sites of oxygen molecule on Pt(100) surface have been tested in our DFT calculations: tht, tbt, htb, btb, hbh and bhb. Details about these geometries have already been given in Section 4.3.2. Table 4.8 lists the adsorption energies for each site and corresponding geometry parameters. It is the tbt site that has the lowest adsorption energy of -1.023 eV which indicates that O_2 will bond to the Pt(100) surface through tbt site. Our results agree well with Panchenko's work [32]. In his work,

the adsorption energy of oxygen molecule at the tbt site is -1.02 eV, where the O-O bond is 1.37 Å and Pt-O bond is 2.02 Å.

Table 4.8 Calculated adsorption energy E_{ad} of oxygen molecule on Pt(100) surface using first principles DFT method

Adsorption Site		tht	tbt	hth	btb	hbh	bhb
E_{ad} (eV)		-0.225	-1.023	0.240	-0.032	-0.050	unstable
Bond	O_1-O_2	1.36	1.36	1.36	1.24	1.24	
Length	O_1-Pt	2.08	2.02	2.09	3.56	5.72	
(Å)	O_2-Pt	2.08	2.02	2.09	3.56	5.18	
Tilting Angle (^{o})		0	0	0	0	25.8	

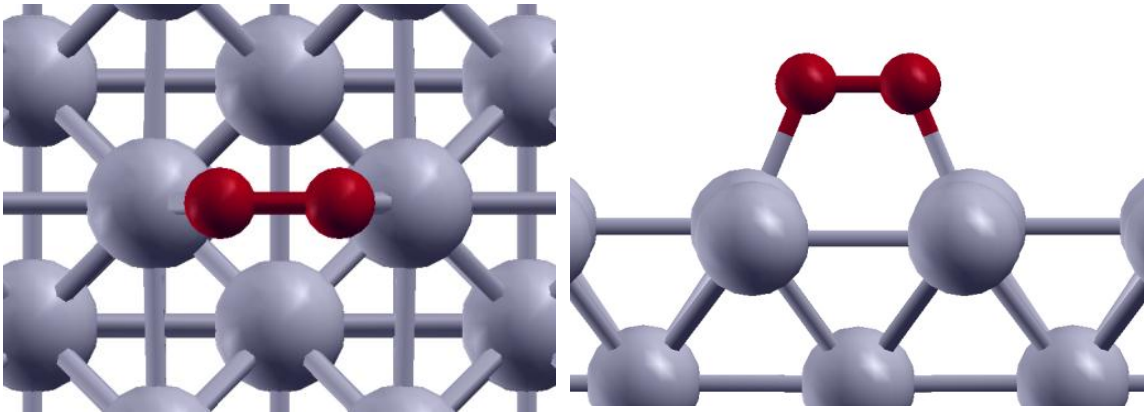

(a) top view (b) side view

Figure 4.14 (a) and (b) Configuration of O_2 adsorption at the tbt site on Pt (100) surface

During the test, we found that bhb site is unstable and the hth site has an adsorption energy larger than zero meaning adsorption of oxygen molecule on this site is impossible to occur. For most cases, the stable configuration would be O-O bond parallel to the surface due to the symmetry consideration. However, it is an exception when

oxygen adsorbed on the hbh site where the tilting angle between O-O bond and (100) surface is 25.8^{o}. Having higher adsorption energy, the hbh site will not be the choice for the O_2 adsorption. Figure 4.14 shows the structure of the adsorbed system of O_2 after geometry optimization.

4.3.5.5 Summary

We carried DFT calculations on the adsorption energy for O, OH, H_2O and O_2 at several high-symmetry sites on the Pt(100) surface. The results show that:

1. For O, the most stable adsorption site is bridge site with the lowest adsorption energy of -3.919 eV.
2. The adsorption of OH molecule is through the O atom binding to the Pt at the bridge site with a 21.2^{o} tilting angle between O-H and Pt(100) surface. The adsorption energy is -2.935 eV for this configuration.
3. When the O atom of H_2O molecule interacts with the Pt atom on the (100) surface through the top site and the whole molecule surface forms an angle of 20.5^{o} with respect to the (100) surface, the adsorption of H2O is most stable.
4. With an adsorption energy of -1.023 eV, the tbt site is the most energetically favorable site among all six high-symmetry sites for the adsorption of O_2 molecule. The O-O bond is stretched to 1.36 Å simultaneously.

4.3.6 Adsorption Energy for (100) Surfaces of Pt-M Catalysts

Based on the conclusion we made in Section 4.3.5.5, for Pt-Ni, Pt-Co and Pt-Fe, the adsorption energy were only investigated at the most stable site on the (100) surface for each species involved in ORR process. The results are listed in Table 4.9. It can be seen that, despite H_2O molecule, for all three other species (O, OH and O_2), the adsorption energy is: Pt > Pt-Ni > Pt-Co > Pt-Fe.

It has been claimed by Stamemkovic et al. [45] that the oxygen adsorption ability can largely affect the ORR activity of catalysts. Generally speaking, the binding energy

between O and Pt is a little bit too strong. The ORR activity will be improved if we find an alloy that can weaken the Pt-O bond, say by about 0.2 eV. According to the results obtained from DFT calculations, the adsorption energy of oxygen on the (100) surface is increased about 0.1eV, 0.2 eV and 0.4 eV for Pt-Ni, Pt-Co and Pt-Fe, respectively, which reflects a weaker binding between O and Pt atoms, and as we mentioned in the Section 2.2, some experiments indeed report better performance of Pt-Ni/Co/Fe alloys than the pure Pt catalyst.

Table 4.9 Adsorption energies (eV) of ORR species on (100) surface for pure Pt and Pt-Ni, Pt-Co and Pt-Fe alloys

Surface	O bridge	OH bridge	H_2O top	O_2 tbt
Pt	-3.919	-2.935	-0.307	-1.023
Pt-Ni	-3.845	-2.853	-0.293	-0.830
Pt-Co	-3.690	-2.708	-0.308	-0.624
Pt-Fe	-3.574	-2.607	-0.302	-0.506

As we discussed before, the degree of interaction of OH and O_2 with different catalyst surfaces is an important indication of their efficiency toward oxygen reduction. The strong binding of OH on the catalyst surface will block the active sites for O_2 adsorption and relative electron transfer; whereas it is generally suggested that O-O bond breaking in O_2 is a key elementary step in determining the reaction dynamic in ORR in acidic solution. As found in DFT calculations, the adsorption energy of OH and O_2 are both larger on the Pt-M alloys' surface than on the pure Pt surface. Therefore it is understandable that in acidic environment these Pt-based alloys have a higher catalytic activity than pure Pt in promoting the ORR. The H_2O adsorption is not distinguishing on all catalysts' surface.

4.3.7 Comparison of (111) Surface and (100) Surface

In order to compare the adsorption energy for (111) and (100) surface, Table 4.10 summarizes the results we obtained by VASP for the species involving ORR process on these two surfaces. This table is combination of Table 4.4 and Table 4.8.

Table 4.10 Comparison of adsorption energies (eV) of ORR species of (111) surface and (100) surface

	O		OH		H_2O		O_2	
	(111)	(100)	(111)	(100)	(111)	(100)	(111)	(100)
Pt	-3.967	-3.919	-2.384	-2.935	-0.287	-0.307	-0.655	-1.023
Pt-Ni	-3.502	-3.845	-2.153	-2.853	-0.237	-0.293	-0.277	-0.830
Pt-Co	-3.378	-3.690	-2.217	-2.708	-0.261	-0.308	-0.274	-0.624
Pt-Fe	-3.191	-3.574	-2.098	-2.607	-0.225	-0.302	-0.186	-0.506

As can be seen in Table 4.10, the corresponding adsorption sites for O, OH, H_2O and O_2 on the (111) surface are fcc, top, top and tbt, respectively; while the adsorption sites regarding to (100) surface are bridge, bridge, top and tbt, respectively.

1) Atomic O adsorption

   For atomic oxygen, stronger binding ability of O to Pt shows on the (111) surface of pure Pt catalyst than the (100) surface. While for the Pt-based alloys (Pt-Ni, Pt-Co and Pt-Fe), the oxygen is more stable adsorbed on the (100) surface.

2) OH adsorption

   It is clear that for all four catalysts, OH adsorbs more strongly on (100) surface with more negative adsorption energy, which explain in some degree why the (100) surface has lower ORR activity in the acid media

3) O_2 adsorption

   Except for the pure Pt catalyst, O_2 molecule shows a strong tendency of adsorption on (100) surface. Again, it indicates the (100) surface may exhibit

lower catalytic activity for ORR process, whereas the situation reverses for pure Pt.

5. CONCLUSIONS AND RECOMMENDATIONS

5.1 Conclusions

We have investigated the surface segregation phenomenon in Pt-Ni and Pt-Co bimetallic alloys using a quantitative approach. In our work, we combined modified embedded atom method for energy evaluation and the Monte Carlo simulation method as the model of statistical mechanics.

From our simulation, we found that: (1) For Pt-Ni and Pt-Co (111) surface, the Pt atoms segregate to the outermost and third layers while Ni/Co atoms segregate to the second atomic shell. Particularly in Pt-rich slab, a nearly pure Pt outermost surface layer can be obtained; (2) On the Pt-Ni (110) surface, a different "surface-sandwich structure" is exhibited with Ni atoms enriched in the first and third layer atomic shell while the Pt is inclined to segregate to the subsurface layer; (3) The surface segregation phenomenon for Pt-Ni (110) (1x2) missing row is similar to the (111) surface with a "sandwich" structure in which Pt atoms are enriched in the outmost layer. As the temperature increase from 1000 K to 1400 K, the tendency of segregation becomes weak. By examining the relaxation of the interlayer distance, we found the interlayer space between the first layer and second layer for Pt-Ni (111) surface is stretched, and the distance between second and third atomic layers is contracted, whereas the situation is reversed for Pt-Ni (110) surface. As for the (110) (1x2) missing row, distances between each of the first three atomic layers are compressed. The results obtained in our simulation agree well with previously experimental work and theoretical calculations and successfully explain why Pt-Ni alloy has a competitive performance compared with pure Pt catalyst in fuel cells, especially PEMFC. With this promising approach to predict surface segregation

phenomenon, we can design alloy catalysts in which precious and high catalytic activity component to be enriched in the outermost surface.

After investigation of surface segregation, we furthered our research on the ORR process for PEMFC in acidic environment through adsorption energy calculations. The adsorption energies of the different species involved in ORR process on Pt and three Pt-based alloys (Pt-Ni, Pt-Co and Pt-Fe) have been fully investigated based on the framework of first principles. Specially, we applied surface segregation phenomenon by building a pure Pt skin on the surface of these alloys. For (111) surface, when adsorbed with O, OH, H_2O and O_2, the most stable configurations are fcc, bridge/top, top and tfb, while bridge, bridge, top and tbt for (100) surface. By comparing the adsorption energies of OH and O_2 on the surface of pure Pt and Pt-base alloys, its relationship to catalytic activity in acidic environment were demonstrated. Also, we found the ORR activity is lower on the (100) surface than on the (111) surface where the adsorption energy of OH and O_2 are higher. This exploration may help to investigate the ORR mechanism on various surfaces and explain the enhanced catalytic performance for Pt-Ni, Pt-Co and Pt-Fe in the cathode.

5.2 Recommendations for Future Research

Future work could be done to expand the current thesis. Divided into two aspects, recommendations on further research are described as follows:

1) Surface Segregation

For Pt-Co alloys, the surface segregation on unreconstructed and reconstructed (110) can be further investigated. Since we introduced surface segregation for Pt-Fe alloy in the DFT calculations, the MEAM potential for Pt-Fe alloy need to be developed and be applied with MC simulations to study the surface segregation phenomenon. Moreover, we haven't study the surface segregation for (100) surface where the adsorption of ORR species was studied. So the (100) surface should be included in the future work.

2) ORR mechanism

We found out the stable configurations and calculated the corresponding adsorption energies for the species involved in ORR process in acidic environment. To fully understand the ORR mechanism, the transition state calculations have to be carried out by VASP coupled with Nudged Elastic Band (NEB) method to find the reaction path.

3) Stability

Although it was found Pt enriched surface in Pt-based alloys, which may improve the catalytic activity and lower the Pt load in catalysts, the stability of keeping this kind of structure during the reaction is still questionable. The next step to complete the research is to investigate the surface structure and property under the working environment.

LIST OF REFERENCES

LIST OF REFERENCES

[1] R. O'Hayre, S. W. Cha, W. Colella, and F. B. Prinz, *Fuel Cell Fundamentals*: John Wiley, 2006.

[2] "Leading the way in the development of automated manufacturing processes for fuel cells." http://fuelcell-igert.rpi.edu/update.do?artcenterkey=24. Last accessed May 2010.

[3] J. Zhang, *PEM Fuel Cell Electrocatalysts and Catalyst Layers*. Springer, 2008, p. 292.

[4] J. K. Norskov, J. Rossmeisl, A. Logadottir, and L. Lindquvist, "Origin of the overpotential for oxygen reduction at a fuel-cell cathode," *Journal of Physical Chemistry B,* vol. 108, pp. 17886-17892, 2004.

[5] V. P. Zhdanov and B. Kasemo, "Kinetics of electrochemical O_2 reduction on Pt," *Electrochemistry Communications,* vol. 8, pp. 1132-1136, 2006.

[6] J. Zhang, *PEM Fuel Cell Electrocatalysts and Catalyst Layers*. Springer, 2006, p. 89.

[7] M. Prutton, *Introduction to Surface Physics*. New York: Oxford University Press, 1994.

[8] Y. Gauthier, Y. Joly, R. Baudoing, and J. Rundgren, "Surface-sandwich segregation on nondilute bimetallic alloys: $Pt_{50}Ni_{50}$ and $Pt_{78}Ni_{22}$ probed by low-energy electron diffraction," *Physical Review B,* vol. 31, pp. 6216-6218, 1985.

[9] Y. Gauthier and R. Bauoding, "Surface-sandwich segregation and multilayer relaxation on $Pt_{0.5}Ni_{0.5}$(110) measured by low-energy electron diffraction: An observation of face-related segregation reversal," *Physical Review B,* vol. 35, pp. 7867-7878, 1987.

[10] Y. Gauthier and R. Baudoing, "Influence of the transition metal and of order on the composition profile of $Pt_{80}M_{20}$(111) (M = Ni, Co, Fe) alloy surfaces: LEED study of $Pt_{80}Co_{20}$(111)," *Surface Science,* vol. 276, pp. 1-11, 1992.

[11] R. Baudoing-Savois, Y. Gauthier, and W. Moritz, "Segregation and ordering at the (1x2) reconstructed $Pt_{80}Fe_{20}$(110) surface determined by low-energy electron diffraction," *Physical Review B,* vol. 44, pp. 12977-12990, 1991.

[12] A. V. Ruban, H. L. Skriver, and J. K. Norskov, "Surface segregation energies in transition-metal alloys," *Physical Review B,* vol. 59, pp. 15990-16000, 1999.

[13] I. A. Abrikosov, A. V. Ruban, H. L. Skriver, and B. Johansson, "Calculated orientation dependence of surface segregations in $Pt_{50}Ni_{50}$," *Physical Review B,* vol. 50, pp. 2039-2042, 1994.

[14] M. Lundberg, "Surface segregation and relaxation calculated by the embedded-atom method: Application to face-related segregation on platinum-nickel alloys," *Physical Review B,* vol. 36, pp. 4692-4699, 1987.

[15] H. Stadler, W. Hofer, M. Schmid, and P. Varga, "Embedded-atom method calculations applied to surface segregation of Pt-Ni single crystals," *Surface Science,* vol. 287-288, pp. 366-370, 1993.

[16] B. Legrand, G. Treglia, and F. Ducastelle, "Phase transitions in surface segregation of Pt_cNi_{1-c} alloys from tight-binding ising-model calculations," *Physical Review B,* vol. 41, pp. 4422-4434, 1990.

[17] C. Creemers, P. Deurinck, S. Helfensteyn, and J. Luyten, "Segregation and ordering at alloys surfaces: modelling and experiment confronted," *Applied Surface Science,* vol. 219, pp. 11-27, 2003.

[18] A. U. Nilekar, A. U. Nilekar, and M. Mavrikakis, "Surface segregation energies in low-index open surfaces of bimetallic transition metal alloys," *Surface Science,* vol. 603, pp. 91-96, 2009.

[19] Y. Ma and P. B. Balbuena, "Pt surface segregation in bimetallic Pt_3M alloys: A density functional theory study," *Surface Science,* vol. 602, pp. 107-113, 2008.

[20] S. Mukerjee and S. Srinivasan, "Enhanced electrocatalysis of oxygen reduction on platinum alloys in proton exchange membrane fuel cells," *Journal of Electroanalytical Chemistry,* vol. 357, pp. 201-224, 1993.

[21] G. Tamizhmani and G. A. Capuano, "Improved electrocatalytic oxygen reduction performance of platinum ternary alloy-oxide in solid-polymer-electrolyte fuel cells," *Journal of the Electrochemical Society,* vol. 141, pp. 968-975, 1994.

[22] T. Toda, H. Igarashi, H. Uchida, and M. Watanabe, "Enhancement of the electroreduction of oxygen on Pt alloys with Fe, Ni, and Co," *Journal of the Electrochemical Society,* vol. 146, pp. 3750-3756, 1999.

[23] U. A. Paulus, A. Wokaun, and G. G. Scherer, "Oxygen reduction on carbon-supported Pt-Ni and Pt-Co alloy catalysts," *The Journal of Physical Chemistry,* vol. 106, pp. 4181-4191, 2002.

[24] Y. Wang and P. B. Balbuena, "Roles of proton and electric field in the electroreduction of O_2 on Pt(111) surfaces: Results of an Ab-initio molecular dynamics study," *The Journal of Physical Chemistry,* vol. 108, pp. 4367-4384, 2004.

[25] D. C. Ford, Y. Xu, and M. Mavrikakis, "Atomic and molecular adsorption on Pt(111)," *Surface Science,* vol. 587, pp. 159-174, 2005.

[26] J. M. Hawkins, J. F. Weaver, and A. Asthagiri, "Density functional theory study of the initial oxidation of the Pt(111) surface," *Physical Review B,* vol. 79, pp. 125434-125447, 2009.

[27] Y. Xu, A. V. Ruban, and M. Mavikakis, "Adsorption and dissociation of O_2 on Pt-Co and Pt-Fe alloys," *Journal of the American Chemical Society,* vol. 126, pp. 4717-4725, 2004.

[28] M. T. M. Koper and R. A. Van Santen, "Interaction of H, O and OH with metal surfaces," *Journal of Electroanalytical Chemistry,* vol. 472, pp. 126-136, 1999.

[29] A. Michaelides and P. Hu, "A density functional theory study of hydroxyl and the intermediate in the water formation reaction on Pt," *Journal of Chemical Physics,* vol. 114, pp. 513-519, 2001.

[30] P. S. Moussounda, M. F. Haroun, and P. Legare, "Adsorption of methanol and atomic oxygen on the Pt(100) surface: a first-principles periodic density functional theory study," *Physica Scripta,* vol. 81, 2010.

[31] G. A. Benesh and L. S. G. Liyanage, "The surface electronic structure of oxygen on Pt(001)(1×1)," *Surface Science,* vol. 261, pp. 207-216, 1992.

[32] A. Panchenko, M. T. M. Koper, T. E. Shubina, and E. Roduner, "Ab initio calculations of intermediates of oxygen reduction on low-index platinum surfaces," *Journal of the Electrochemical Society,* vol. 151, pp. A2016-A2027, 2004.

[33] M. I. Baskes, "Modified embedded-atom potentials for cubic materials and impurities," *Physical Review B,* vol. 46, pp. 2727-2742, 1992.

[34] M. I. Baskes and R. A. Johnson, "Modified embedded-atom potentials for hcp metals," *Modelling and Simulation in Materials Science and Engineering,* vol. 2, pp. 147-163, 1994.

[35] J. H. Rose, J. R. Smith, F. Guinea, and J. Ferrante, "Universal Features of The Equation of State of Metals," *Physical Review B,* vol. 29, p. 2963, 1984.

[36] M. I. Baskes, "Determination of Modified Embedded Atom Method Parameters for Nickel," *Materials Chemistry and Physics,* vol. 50, pp. 152-158, 1997.

[37] M. I. Baskes, "Atomistic potentials for the molybdenum-silicon system," *Materials Science and Engineering A,* vol. 261, pp. 165-168, 1999.

[38] W. B. Pearson, *A Handbook of Lattice Spacings and Structures of Metals and Alloys,* 1st ed. New York: Pergamon, 1964.

[39] P. Novacek, E. Taglauer, and P. Varga, "Analysis of the surface of Pt_xNi_{1-x} alloys," *Journal of Analytical Chemsitry,* vol. 341, pp. 136-139, 1991.

[40] Y. Gauthier, R. Baudoing-Savois, J. J. W. M. Rosink, and M. Sotto, "LEED study of $Pt_{25}Co_{75}$(111)," *Surface Science,* vol. 297, pp. 193-201, 1993.

[41] W. Khon and L. Sham, "Self-consistent equations including exchange and correlation effects," *Physical Review A,* vol. 140, 1965.

[42] T. Jacob, P. M. Richard, and A. G. William, "Chemisorption of atomic oxygen on Pt(111) from DFT studies of Pt-clusters," *The Journal of Physical Chemistry B,* vol. 107, pp. 9465-9476, 2003.

[43] A. Eichler, F. Mittendorfer, and J. Hafner, "Precursor-mediated adsorption of oxygen on the (111) surfaces of platinum-group metals," *Physical Review B,* vol. 62, pp. 4744-4755, 2000.

[44] Q. Ge, P. Hu, and D. A. King, "Site symmetry dependence of repulsive interactions between chemisorbed oxygen atoms on Pt{100}(1x1)," *Journal of Chemical Physics,* vol. 106, pp. 1210-1215, 1996.

[45] V. Stamenkovic, B. S. Mun, K. J. J. Mayrhofer, and P. N. Ross, "Changing the activity of electrocatalysts for oxygen reduction by tuning the surface electronic structure," *Angewandte Chemie-International Edition,* vol. 45, pp. 2897-2901, 2006.